

Distortion Correction and Momentum Representation of Angle-Resolved Photoemission Data

Jonathan Adam Rosen

B.Sc., University of California at Santa Cruz, 2006

A THESIS SUBMITTED IN PARTIAL FULFILLMENT OF
THE REQUIREMENTS FOR THE DEGREE OF

MASTER OF SCIENCE

in

THE FACULTY OF GRADUATE STUDIES

(Physics)

THE UNIVERSITY OF BRITISH COLUMBIA

(Vancouver)

October 2008

Abstract

Angle Resolved Photoemission Spectroscopy (ARPES) experiments provides a map of intensity as function of angles and electron kinetic energy to measure the many-body spectral function, but the raw data returned by standard apparatus is not ready for analysis. An image warping based distortion correction from slit array calibration is shown to provide the relevant information for construction of ARPES intensity as a function of electron momentum. A theory is developed to understand the calculation and uncertainty of the distortion corrected angle space data and the final momentum data. An experimental procedure for determination of the electron analyzer focal point is described and shown to be in good agreement with predictions. The electron analyzer at the Quantum Materials Laboratory at UBC is found to have a focal point at cryostat position 1.09mm within 1.00 mm, and the systematic error in the angle is found to be 0.2 degrees. The angular error is shown to be proportional to a functional form of systematic error in the final ARPES data that is highly momentum dependent.

Table of Contents

Abstract.....	ii
Table of Contents.....	iii
List of Tables	v
List of Figures.....	vi
List of Illustrations.....	vii
Acknowledgements.....	ix
Chapter 1 Introduction to Angle Resolved Photoemission Spectroscopy	1
UBC ARPES Chamber Experimental Apparatus	4
Chapter 2 Practice of Angular Distortion Correction.....	5
Distortion Correction from Slit Correction Data	6
Chapter 3 Calculations Near Ideal Geometry	10
Approximations for the Angle Between Extreme Iso-Angle Contours	15
Deviation of Point Source Position from the Optical axis.....	18
Calculation of Errors in the Nearest Central Iso-Angle Contour Approximation	21
Chapter 4 Image Warping.....	26
Procedure of Finding Peak Positions in Slit Correction Data.....	28
Final Positions to Construct the Discreet Coordinate Mapping Function	30
Fitting of the Mapping Function	31
The Conservation of Spectral Weight.....	31
Extensions in Two Dimensions.....	34
Chapter 5 Experimental Procedure for Determining the Focal Point.....	35
Post Distortion Correction Detector Angle Axis	38
Propogation of uncertainty in the detector angle axis.....	39
Implementation Distortion Correction for the UBC ARPES Chamber	40

Chapter 6 Mapping to Momentum	41
Rotation Transformation and Solving Momentum	43
Angles from Momentum	48
Cryostat Phi Resolution	49
Effect of Angular Uncertainty on Momentum Coordinates.....	49
Chapter 7 Conclusions and Future Applications	53
References.....	55
Appendix A.....	56
Appendix B.....	59
Appendix C.....	60

List of Tables

Table 3.1 Discontinuity Positions of Delta for Several Analyzer Modes.....17

List of Figures

Figure 2.1.	Raw Data from a Slit Array Calibration Experiment	7
Figure 2.2.	Selected Iso-Energy Cuts of the Slit Correction Data.....	8
Figure 3.1.	Functional Form of Delta.	17
Figure 4.1.	The Application of Peak Finding	29
Figure 5.1.	Energy -Averaged Photoemission Signal.....	35
Figure 5.2.	Uncorrected ARPES Images Versus Cryostat Position.	36
Figure 6.1.	Vector Plots of Momentum	47
Figure 6.2.	The Error in Momentum Coordinates	51

List of Illustrations

Illustration 3.1.	The slit correction experiment geometry	11
Illustration 6.1.	Definition of electron emission coordinates.	41
Illustration 6.2.	Definition of the detector angle and the cryostat angles	42
Illustration C.1.	Energy Direction Cropping	61
Illustration C.2.	Angular Direction Cropping.....	62
Illustration C.3	Result of the Crop Settings.....	63
Illustration C.4.	Energy Region for Fitting Contours	64
Illustration C.5.	Result of Fitting the Contours.	65
Illustration C.6.	Rendering of the Slit Correction Data.....	66
Illustration C.7.	The Distortion Correction Applied to ARPES Data.....	67

List of Abbreviations

ADP – Approximation Deviation Parameters

ARPES – Angle Resolved Photoemission Spectroscopy

DFED – Distortion Free Energy Detection

HAD – High Angular Dispersion

IAC – Iso-Angle Contours

IEC – Iso-Energy Contours

IPO – Image Parameter Orthogonality

LAD – Low Angular Dispersion

NCIACA – Nearest Central Iso-Angle Contour Approximation

SCD – Slit Correction Data

UBC – University of British Columbia

WAM – Wide Angle Mode

Acknowledgements

I would like to thank Andrea Damascelli, Nick Ingle, David Fournier, Giorgio Levy, Christian Veenstra, and Ryan Wicks for valuable conversations and assistance with project.

Chapter 1 Introduction to Angle Resolved Photoemission Spectroscopy

Angle resolved photoemission spectroscopy (ARPES) is a powerful experimental probe of the elementary excitations of electrons in solid-state materials. At the most basic level it is a procedure of illuminating a material with energetic photons, and studying the angular and energy distribution of electrons that come out of the material surface. Some of the properties of electrons that are ejected from the sample material are directly related to the properties those electrons possessed in bound-states of the material, and this information can be extracted in this type of experiment. ARPES allows us to better understand the properties of the electrons in materials.

The fundamental parameters of detection in ARPES exist in a four-dimensional object, which is a map of intensity as function of two angles and kinetic energy. Intensity in this experiment is a function formed by the many body spectral function weighted by a Fermi-Dirac distribution, and the probability function formed by the square of the matrix element of the interaction Hamiltonian with the many body initial and final states¹. In the case where the spectral function is analytic, first order perturbations show that the many body spectral function is analogous to a renormalized single-particle spectral function², and in this situation ARPES intensity is proportional to the single-particle electron density of states with some shifts and broadening brought about by the perturbation of many-body interactions.

The cross-section for the absorption of photons depends on the material and the photon energy, but of even higher importance to ARPES is the electron mean free path in the material. In practice, it is always the case in an ARPES experiment that the electron escape depth is the limiting factor in the detection of photo emitted electrons from the bulk material. Studies have been done to show that the escape depth of electrons varies with photon energy, and that in the range of angle-resolved ultraviolet photoemission the escape depth is about five to ten angstroms³. For this reason, ARPES is generally considered to be a surface-sensitive technique that largely probes the electron energy states that occur in spatial vicinity to the material surface.

¹ Damascelli, A. 2004. Probing the Electronic Structure of Complex Systems by ARPES. *Physica Scripta* T109: 61-74.

² Mattuck, R. *A Guide to Feynman Diagrams in the Many-Body Problem*. Dover, 1992.

³ Huefner, S. *Photoelectron Spectroscopy*. Springer Verlag, 1995.

In any surface-sensitive experiment, it is important to perform measurements on a surface that is very clean and flat. This is because any impurities that have adhered to the surface have essentially changed the material composition and possibly affected the energy states that the experiment will probe. In addition, any inhomogeneity of the surface will result in the detection of electrons that can be considered to have come from a superposition of different surface orientations which will significantly reduce the resolution of the experiment. Surface inhomogeneity can also lead to disruption of the electron energy states (reference) from that of the flat surface. In performing ARPES, it is important to study a material surface that is as close to being atomically flat (reference) as possible, and in order to reduce impurities it should be done in a high vacuum environment³.

Among the most interesting and useful quantities obtained in photoemission spectroscopy is the photoelectron emission angle, which is the angle at which the electron is ejected from the material, relative to its surface. The emission angle can be used to determine the in-plane crystal momentum of the electron in the sample material, due to the invariance of translational symmetry across the sample surface of the component of momentum parallel to the surface¹.

This can be seen to be a special case of Noether's theorem, which proves that when a quantity invariant under a transformation occurs in the Hamiltonian, the corresponding generalized conjugate momentum is conserved⁴. For the photoemission problem, the Hamiltonian contains a spatially varying potential $V(x, y, z)$ which describes the crystal bulk, surface, and vacuum. If we take the perfectly flat material surface to lay in the y - z plane, then inside the material the potential obeys relation,

$$V(x, y, z) = V(x, y + r_y, z + r_z)$$

for any direct lattice vector $\vec{r} = r_y \hat{j} + r_z \hat{k}$. This symmetry is not present along the coordinate x because of the discontinuity of the potential at the material vacuum interface. It is a well known that the infinite periodic potential in the crystal allows the solutions of Bloch states for the electron wave equation, hence the designation of crystal momentum to parameterize these states. The essential use of Noether's theorem for photoemission is to

⁴ Goldstein, H. Classical Mechanics (3rd Edition). Addison Wesley, 2001.

recognize that the y-z plane translation symmetry means that the momentum analog in the Hamiltonian, the crystal momentum, is conserved for the y and z coordinates but not for the x coordinate. Once the electron has left the material and entered the vacuum, the freely propagating electron has momentum and kinetic energy given by,

$$\vec{p} = \hbar \vec{k}$$

$$E_K = \frac{p^2}{2m} = \frac{\hbar^2}{2m} (k_x^2 + k_y^2 + k_z^2)$$

Neither of these quantities is equal to the electron momentum and energy when it was inside the crystal, because while k_y and k_z are conserved across the interface, k_x is not. In addition to momentum, there is energy conservation for photon $h\nu$ and material work function ϕ in the non-interacting picture¹ where one strictly considers elastic processes.

$$E_K = h\nu - \phi - |E_B|$$

As result of momentum and energy conservation ARPES probes the spectral function in the k_y - k_z plane of the reciprocal crystal - but the detected kinetic energy is not independent of k_x , and the measured k_x of the emitted electron is not the same as for the electron in the solid.

Full knowledge of the crystal momentum can be put together with energy detection of the electrons in order to gain information on the single-particle band structure. Since the component of momentum perpendicular to the material surface is not conserved, this is sufficient reason restrict the general discussion to materials that possess a highly anisotropic electron overlap and can be considered to have no energy dispersion in one dimension. This is the class of two dimensional electronic materials, mainly composed of three dimensional crystals that have very weak coupling in one direction¹. While ARPES can produce valuable insights into the nature of fully three dimensional electron systems, these must often proceed somewhat differently on a case by case basis due to the basic spatial symmetry of the surface and the complex differences in single-particle excitation spectrums and band structure for each material. The discussions and procedures developed in this work are primarily intended for study of two dimensional electronic materials and the scope will be limited to such materials.

Further discussion of the results of ARPES are not necessary at this point, because the wealth of information one can obtain from this probe of the many-body system is truly the endpoint of this work, and the pieces will be included as needed for the complete discussion. In order to obtain information on material's Fermi surface or other interesting material physics, a significant amount of pre-analysis treatment and calculations is vital. In real data acquisition, the raw data is not ready for analysis. The subject of this project is to completely describe and quantify the extraction of relevant information. This will take place via the transformation of the raw image data acquired in an ARPES experiment to a corollary rendered form - with well defined parameters to describe accuracy and precision.

UBC ARPES Chamber Experimental Apparatus

The experimental basis of this work utilized the facilities at Quantum Materials Laboratory in the Brimacombe Building at the University of British Columbia. Of specific interest to this body of work is the component of the Quantum Materials Laboratory facility that is specifically designed for ARPES, in addition to calibration apparatus and other analog machinery and digital devices that serve a complementary function to the ARPES experiment. Details about these components can be found in appendix A.

Chapter 2 Practice of Angular Distortion Correction

The Phoibos 150 hemispherical analyzer is equipped with both straight and curved entrance slits. The primary focus of this work is based on the use of an entrance slit that has twice the curvature of the hemisphere, which is a feature that is intended to compromise between energy resolution and electron lens distortion. The reason for this is that it simplifies the way in which electron impact events are detected by reducing the curvature of iso-energy contours on the ccd camera images. This greatly simplifies the pre-analysis correction of ARPES data, although it results in somewhat reduced resolution because of the broader distribution of electrons across the hemispherical capacitor entrance.

One important implication of this entrance slit configuration is that the axis of energy detection on the phosphor screen as seen by the camera system is made to be as straight as possible. This situation can be described as “distortion-free” energy detection (DFED), where iso-energy contours on the ccd camera form lines parallel to one axis of the square ccd pixel array. DFED is a useful tool to simplify the analysis of raw images from the detection system, because it eliminates the need to parameterize energy contours.

In the DFED, the energy-axis is as close to straight as possible, but the trajectories of iso-angle contours (IAC) are not parallel to either axis of the ccd array. The deviation of the IAC parameterization from the line parallel to the axis of the ccd array which is perpendicular to the DFED axis is typically described as angular distortion, and the process by which this complication is resolved is referred to here as distortion correction.

The approach to achieve distortion correction in this body of work started with quantification of the angular distortion, proceeding first with the parameterization of iso-angle curves as a function of energy. This requires a special kind of experimental configuration, to achieve well-defined IAC on the ccd camera. This experiment is readily done in the UBC ARPES system, with a built-in slit array that can be placed in front of the analyzer entrance, a vertical tungsten wire on the lowest part of the cryostat, and an electron gun. The experiment involves bombarding the tungsten wire with electrons of a broad energy range much larger than the energy range passed into the analyzer.

The tungsten wire is an almost perfect point source for the analyzer’s angular acceptance of electrons that are scattered or emitted from the wire, since the difference in angle from either side of the wire is negligible. The photoelectrons enter the analyzer through

the slit array, which has twenty one slits of size 0.13mm, which are spaced 1mm apart, cut into a flat aluminum disk and oriented perpendicular to the angular acceptance of the analyzer. Conducting this experiment allows the direct detection of IAC. There are several other parameters involved, though, including the position of the wire, the position of the slit array, and the position of the electron gun.

The ideal geometry has the tungsten wire is exactly on the optical axis, defined as the axis that passes through the center of the analyzer entrance and is normal to the plane of the entrance. In addition, the electron gun should illuminate the position on the wire that forms the perpendicular intersection of the wire and optical axis, and the center slit of the slit array should be centered on the optical axis. For a number of reasons, however, the likelihood of this situation occurring exactly is minimal, and some offset in these positions is inevitable. This will introduce some experimental errors, which will be quantified in the next section.

Distortion Correction from Slit Correction Data

The underlying principle of distortion correction is that intensity values occur at the incorrect position on the ccd camera from the perspective of data analysis, and reassignment of the intensity to new positions is needed for the attribution of physical information such as momentum and spectral density. The best solution to this problem is to find a way to accurately move the intensity to new positions that are determined in the coordinate space in which the detection quantities of angle and energy form perpendicular axes. This solution is useful primarily because it renders the detected information in a space where the variables of detector angle and kinetic energy are parameterized by independent mutually perpendicular directions which are coincident with the directions that define the symmetry of individual detection elements, or pixels, in relation to one another on the ccd camera. This ideal situation, referred to here as image parameter orthogonality (IPO), greatly simplifies the analysis of data, because it allows the immediate interpretation of ARPES data as intensity as a function of angle and kinetic energy. IPO allows the straightforward use of ARPES data to construct additional physical quantities such as electron momentum, Fermi velocity, and self-energy, whereas the raw images acquired on the detector in an experiment are not readily interpreted in this way even with DFED, because of the unknown energy dependence of the detector angle.

To attain ARPES data with IPO from the raw detection images, an accurate function is

needed which parameterizes the new positions of the intensity function by the original positions. This function is a map from old coordinates to new ones, in such way that the correct position of each intensity value on the ccd camera can be calculated from the original positions accompanying the intensity of the raw image, once the mapping function is known. To obtain the mapping function, however, very specific quantitative information must be collected from slit correction data (SCD) taken in a suitable experiment with the slit array, and it must be done in such a way that it remains valid for application to a separate ARPES experiment done on a material surface of interest.



Figure 2.1. The raw data from a slit array calibration experiment. The left to right direction is parallel to the energy axis, while the up to down direction is roughly the angle axis. If the angular axis is straight, then the lines will be straight, so angle distortion is apparent in the curvature.

A successful calibration experiment will produce data like that shown in figure 2.1, containing the positions of IAC. In the case of DFED, each column of a detector image that corresponds to a single kinetic energy can be treated separately in the quantification of angular distortion.

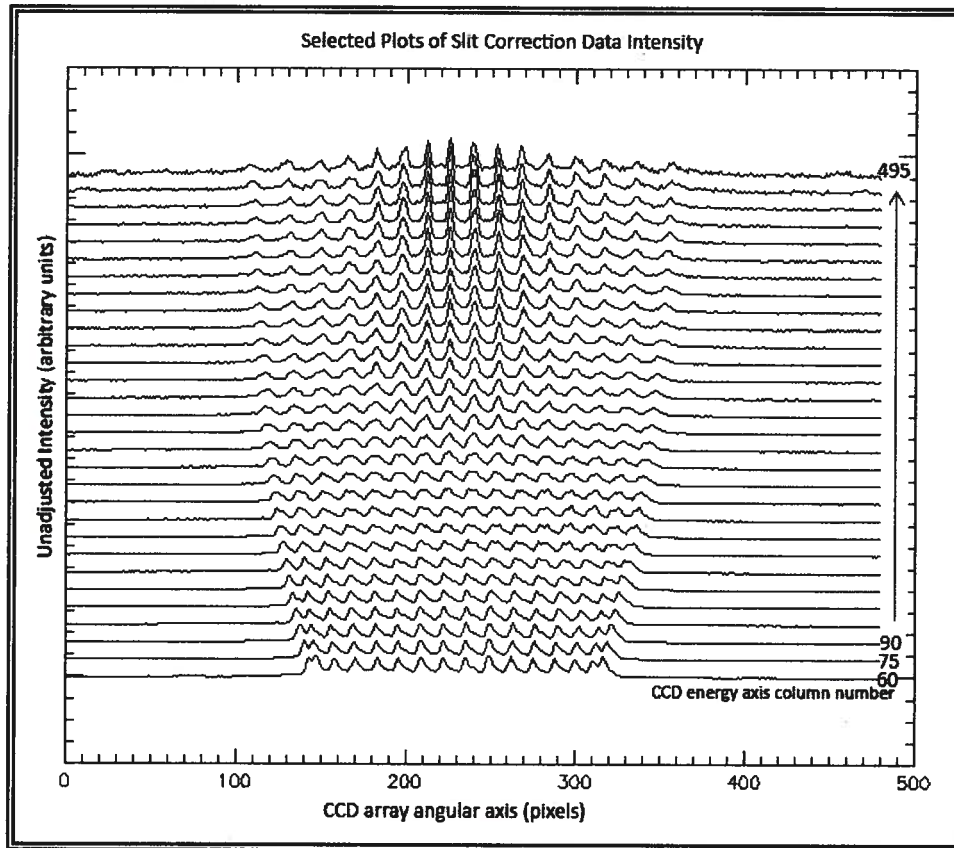


Figure 2.2. Selected iso-energy cuts of the slit correction data, labeled by ccd energy axis column number. These are functions of intensity and are plotted versus the ccd angular axis. The angular distortion can be quantitatively characterized from the peak positions in each energy cut.

In the slit correction data, for each column we have a number of positions less than the column size, which coincide with electron emission angles. The known peak positions come from the IAC that pass through the column, as seen in figure 2.2, and the SCD column with peak positions contains sufficient information to characterize angular distortion.

The destination coordinates for the IAC lay on a linear angle axis described by an offset and slope. The slope is the rate of change of pixels on the IPO image with changing detection angle of electron emission, and can be defined as γ in units of pixels per angle. The offset corresponds to merely shifting all of the final coordinates by some constant. In terms of the detector images, γ will produce a stretch/shrink along the ccd axis perpendicular to the energy axis, while the constant will simply translate the image along this direction. For this reason, the constant is irrelevant to the transformation and we can take it to be zero.

The instantaneous slope of the function that returns the angle at each pixel in the

original image is both a function of energy and angle in our system. For the final coordinates γ can be chosen to be anything, since the final image has a linear angle axis and because pixels are not a physical quantity - they are only meaningful in their relation to the physical quantities of angle and energy. An appropriate and reasonable choice of γ corresponds to the number of pixels per angle in the center of the SCD image, with the number of pixels between the largest and smallest peak positions for the center column divided by the angle between these two peaks. In this way γ is chosen to be close to the average pixel per angle ratio of the raw ARPES data, but it should be realized that this is only a matter of convenience and does not have any effect on physical information contained in the image.

Briefly it should be mentioned that choosing γ that is very small compared to the intrinsic resolution of the ARPES system will result in data that displays a lower resolution than what is possible. If γ is instead chosen to be very large, this will give an angle axis that has much smaller interval spacing than could possibly be resolved, though the intensity data itself would show this. These are extreme cases, however, and as long as γ is assigned in the reasonable way described, there will be no significant effect on final data resolution from this parameter.

The pixel per angle parameter can be determined readily due to its minimal effect on the quality of the final data, though it still remains that this parameter alone is insufficient information to complete the distortion correction. Additionally, the determination of the final positions requires knowledge of the central positions that correspond to electron propagation along the optical axis. The approximation scheme for obtaining this information, and the evaluation of the final positions will be the subject of the next chapter.

Chapter 3 Calculations Near Ideal Geometry

The SCD can be used to quantify the axis of the detector angle. This section will demonstrate that it is possible with the UBC ARPES system to observe clear signature of the geometry which yields the most accurate quantification of the detector angle axis, and we can describe the way in which the experimentalist can interpret these signatures as indications of the proximity of the sample and slit array to the ideal position when performing an experiment. It will be assumed in the calculation that the ARPES experiment is executed with the sample or point source close to the focal point of the analyzer. Additionally there will be an assumption of known offset of the slit array which is zero when an odd number of IAC are present in the SCD image, and is half of the inter-slit distance when an even number of IAC is present.

This is equivalent to assuming the IAC nearest the center of the SCD image represent the positions that would be exact if in the ideal configuration, and is referred to as the nearest central iso-angle contour approximation (NCIACA). To assess the accuracy of these assumptions, this work will additionally examine the errors introduced which originate from the positions deviating from those that are assumed. In doing so, the calculation of detector angle will carry a quantifiable error that will lead to the refinement of the experimental procedure to reduce these errors.

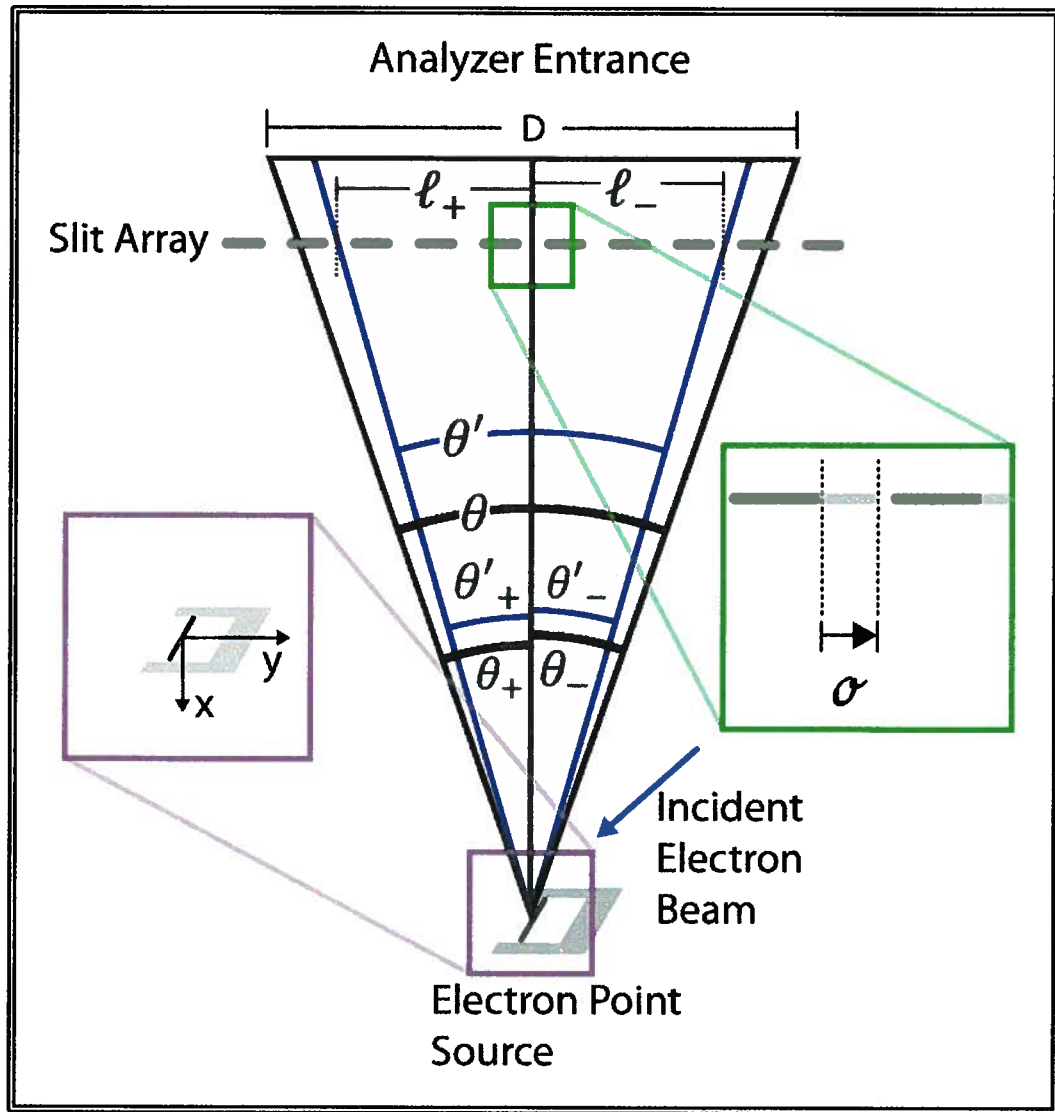


Illustration 3.1. The slit correction experiment geometry, showing the interdependent variables that quantify the positions and angles. Two positions, x and y , describe the point source, σ describes the slit array position, and D is given by the analyzer setting. The rest of the parameters are resultant from the fundamental parameters x , y , σ , D .

To mathematically describe the effect of sample and slit array positions on the SCD, the configuration of illustration 3.1 is used. At this point it is simplest to consider the slits to have infinitesimal width, though this idealization will be lifted later. σ is the offset of the center of a slit from the optical axis. This offset should be taken to be less than or equal to half the slit spacing in absolute value, since there are more slits on the slit array than are visible in SCD images in any angular analyzer mode, and we can take the slit array to be infinite along the direction of detector angle. L_A is the distance from the point source to the analyzer entrance,

L_S is the distance from the point source to the slit array, D is the size of the effective electron acceptance of the analyzer, d is the inter-slit distance, and finally y is the distance of the point source along the direction parallel to the analyzer entrance slit from the focal point in either the positive or negative direction as defined by illustration 3.1 . The variables y and σ quantify deviation from the ideal case embodied by the NCIACA. The parameter D is a property of analyzer lens mode, since different angular modes accept different solid angles of electron emission. D can be deduced from the manufacturer specifications for the solid angle of acceptance of a given lens mode and position of the electron lens focal point relative to the optical axis.

In the case where the SCD is taken in the ideal geometry, the angles are very well known by the geometry of the arrangement of point source and slit array with respect the analyzer entrance and optical axis. The detector angle axis can be closely determined if positions are close to the ideal geometry, but in order to quantify the amount of approximation the ideal case must be compared with the more realistic case of non-ideal positions.

On the SCD image, there are a set of IAC that show the ccd positions corresponding to specific angles, but the values of the angles are not known. In particular we need to know the electron emission angle spanned between the most extremely placed IAC visible, as this is enough to determine γ and will facilitate the creation of the detector angle axis. In the ideal geometry, the extreme IAC on either side of the one (odd number of IAC) or two (even number of IAC) central IAC is symmetric on the detector angle axis, but in general there is some asymmetry when the positions are not ideal.

There are two angles shown in illustration 3.1, θ_+ and θ_- , formed by the construction of two right triangles with shared base along the optical axis, which span the angle on either side of the axis that coincides with the angular acceptance of the analyzer defined by D and L_A . The angles θ_+ , θ_- , and θ are given by,

$$\theta_{\pm} = \tan^{-1} \left[\frac{\frac{D}{2} \pm y}{L_A} \right]$$

$$\theta \equiv \theta_+ + \theta_- = \tan^{-1} \left[\frac{\frac{D}{2} + y}{L_A} \right] + \tan^{-1} \left[\frac{\frac{D}{2} - y}{L_A} \right] \quad (3.1)$$

When the slit array is placed in front of the analyzer entrance, a set of IAC are selected.

The angle between the extreme IAC is not θ in illustration 3.1, but rather θ' . This effect is best quantified by counting lines. If there are n_1 slits to the left of the slit nearest the point source, for which emission angles are less than or equal in absolute value to θ_1 , then the magnitude of the distance between the extreme slit and slit nearest the point source is,

$$\ell_{\pm} = n_1 d \mp \sigma$$

$\theta'_{\pm} \leq \theta_{\pm}$, where these angles are taken to be positive, because the slit array passes electron emission angles only within the effective analyzer acceptance region, so that,

$$\begin{aligned} \tan^{-1} \left[\frac{n_{\pm} d \mp \sigma}{L_S} \right] &\leq \tan^{-1} \left[\frac{\frac{D}{2} \pm y}{L_A} \right] \\ \Rightarrow \frac{n_{\pm} d \mp \sigma}{L_S} &\leq \frac{\frac{D}{2} \pm y}{L_A} \end{aligned}$$

Rearranging this relation produces,

$$n_{1\pm} \leq \frac{1}{d} \left(\frac{L_S}{L_A} \left(\frac{D}{2} \pm y \right) \pm \sigma \right)$$

The number of slits that are passing electrons visible in the SCD is an integer, so long as we neglect the slit width. Even in the real experiments, as long as the the entire IAC is visible in the SCD image, and not just a fraction of its finite width, we can consider n_{\pm} to be integers. This constraint means we can turn the inequalities into exact equations that utilize the floor function. For instance, if the inequality states that n_+ must be less than or equal to 12.7, then it is know that n_+ is equal to twelve, because all of the slits within ℓ_+ from the point source will pass electrons with emission angles that correspond to arrival at the analyzer in the effective acceptance range. This means we can write,

$$n_{\pm} = \text{Floor} \left[\frac{1}{d} \left(\frac{L_S}{L_A} \left(\frac{D}{2} \pm y \right) \pm \sigma \right) \right]$$

Here, the floor function is defined as the function that gives the largest integer less than or equal its argument. With n_{\pm} we can calculate θ' .

$$\theta' \equiv \theta'_+ + \theta'_- = \tan^{-1} \left[\frac{n_+ d - \sigma}{L_S} \right] + \tan^{-1} \left[\frac{n_- d + \sigma}{L_S} \right] \quad (3.2)$$

This equation is elucidated by rewriting n_{\pm} as,

$$\begin{aligned} n_{\pm} &= \text{Floor} \left[\text{Floor} \left[\frac{L_S D}{2dL_A} \right] + \Delta \pm \frac{L_S}{dL_A} y \pm \frac{\sigma}{d} \right] \\ &= \text{Floor} \left[\frac{L_S D}{2dL_A} \right] + \text{Floor} \left[\Delta \pm \frac{L_S}{dL_A} y \pm \frac{\sigma}{d} \right] \\ \Delta &= \frac{L_S D}{2dL_A} - \text{Floor} \left[\frac{L_S D}{2dL_A} \right] \end{aligned}$$

The condition for a change to occur in n_{\pm} is that the quantity $\Delta \pm \frac{L_S}{dL_A} y \pm \frac{\sigma}{d}$ will equal an integer. Additionally, due to the definition as a difference between a quantity and its floor, $\Delta < 1$ and $\text{Floor}[\Delta] = 0$. Defining n to be the portion of n_{\pm} that is independent of y or σ ,

$$\begin{aligned} n &\equiv \text{Floor} \left[\frac{L_S D}{2dL_A} \right] \\ n_{\pm} &\rightarrow n + \text{Floor} \left[\Delta \pm \frac{L_S}{dL_A} y \pm \frac{\sigma}{d} \right] \quad (3.3) \end{aligned}$$

It is clear that when y and σ are equal to zero, n_+ equals n_- , and when they are nonzero, n_+ and n_- will not change at the same values of y and σ unless Δ is zero. This implies that when $\frac{L_S D}{2dL_A}$ is equal to or slightly larger than an integer, Δ is close to zero, and there is high symmetry between n_+ and n_- . This is an interesting result, because the parameters used to calculate Δ are dependent on chamber construction and analyzer lens mode only, so they are essentially fixed numbers in an ARPES experiment. Therefore to the extent that these parameters are known, the symmetry of n_{\pm} will be known with respect to y and σ .

Approximations for the Angle Between Extreme Iso-Angle Contours

Returning to the original assumption of ideal positions, we can now calculate the angle between the extreme IAC, and compare with the exact formula derived in the last section. There are two instances of approximation that must be considered separately. In one case the number of IAC in the SCD is even, and in the other it is odd. If we have an even number of IAC then the position between the central two IAC is taken to correspond to the optical axis, the slit array offset is assigned to $\sigma = d/2$, and $y = 0$ is used since it is assumed that the point source is on the optical axis. In this situation the exact calculation reduces to,

$$n_{\pm} = n + \text{Floor} \left[\Delta \pm \frac{1}{2} \right]$$

$$\theta' = \tan^{-1} \left[\frac{d}{L_S} \left(n + \text{Floor} \left[\Delta + \frac{1}{2} \right] - \frac{1}{2} \right) \right] + \tan^{-1} \left[\frac{d}{L_S} \left(n + \text{Floor} \left[\Delta - \frac{1}{2} \right] + \frac{1}{2} \right) \right]$$

This suggests the definition,

$$n_{\pm}^* \equiv \left(n + \text{Floor} \left[\Delta \pm \frac{1}{2} \right] \mp \frac{1}{2} \right)$$

$$\Rightarrow \theta' = \tan^{-1} \left[\frac{n_{+}^* d}{L_S} \right] + \tan^{-1} \left[\frac{n_{-}^* d}{L_S} \right]$$

The allowed values are in the range $0 \leq \Delta < 1$, in which n_{+}^* and n_{-}^* are equal. To show this, take $\Delta < 1/2$,

$$n_{+}^* \equiv \left(n + 0 - \frac{1}{2} \right) = n - \frac{1}{2}$$

$$n_{-}^* \equiv \left(n - 1 + \frac{1}{2} \right) = n - \frac{1}{2}$$

For $\Delta \geq 1/2$,

$$n_{+}^* \equiv \left(n + 1 - \frac{1}{2} \right) = n + \frac{1}{2}$$

$$n_{-}^* \equiv \left(n - 0 + \frac{1}{2} \right) = n + \frac{1}{2}$$

Both n_{\pm}^* have a discontinuity at $\Delta = 1/2$ where a jump occurs with the size of one. This shows that depending on the size of Δ , it is possible to have either $2n - 1$ or $2n + 1$ IAC

present in the SCD, but the ideal assumptions of zero for y and σ has resulted in the number of IAC changing by two across the point of discontinuity. The SCD image will show these lines symmetrically on either side of the image. In the case where the user of the UBC ARPES chamber is changing the position of the point source along the optical axis, this would result in two IAC appearing or disappearing on either side of the SCD image at the same time, as the parameter Δ passes through the discontinuity point as a function of L_S and L_A .

Now the additional situation must be addressed, in which there are an odd number of IAC in the SCD image. For this case, the NCIACA proceeds by setting both y and σ to zero. This leads to modification of the equations for n_{\pm}^* . In the “odd” case there is no σ , so that there is no longer any difference in of n_{\pm} .

$$n_{\pm} = n_{\pm}^* = n + \text{Floor}[\Delta] = n$$

In this case it is apparent that the discontinuity still results in two lines appearing or disappearing at the edge of the SCD image, though it will occur when $\Delta = 0$ via the definition for n , which is the same as Δ infinitesimally close to one.

It may be useful to understand the situation where the discontinuity of n_{\pm}^* occurs when moving the point source along the optical axis, in that the implementation of assumptions of the NCIACA will cause this movement to appear differently in the SCD image than in the general case. We are interested in the trend in the discontinuity position, which gives a clear signature in the SCD, as a function of the optical axis position relative to the focal point, and at this junction we try to understand this trend within the NCIACA. To simplify the equation for Δ , it can be rewritten in terms of unitless parameters.

$$\Delta = \sigma \left(\frac{\rho + \chi}{1 + \chi} \right) - \text{Floor} \left[\sigma \left(\frac{\rho + \chi}{1 + \chi} \right) \right] ; \sigma \equiv \frac{D}{2d}, \rho \equiv \frac{L_S}{L_A}, \chi \equiv \frac{x}{L_A}$$

The variable x is the distance along the optical axis, as shown in illustration 3.1. In terms of the unitless parameters, some examples of the function Δ can be plotted for different values of σ (representing different lens modes) to get a general idea of the trend in the discontinuity position. ρ can be fixed to 32/40 for this discussion, because this number is given by the geometry of the UBC ARPES chamber, in addition to $\chi = x/40$ with x in

millimeters.

Analyzer Mode	Angular Acceptance	D	σ (d=1mm)	Delta Discontinuity Position Nearest the focal point (χ , even/odd)
HAD	$\pm 3^\circ$	4.19262	2.09631	-0.296907, -0.61757
LAD	$\pm 7^\circ$	9.82276	4.91138	-0.304032, 0.0777874
WAM	$\pm 13^\circ$	18.4695	9.23473	0.0646891, -0.173525

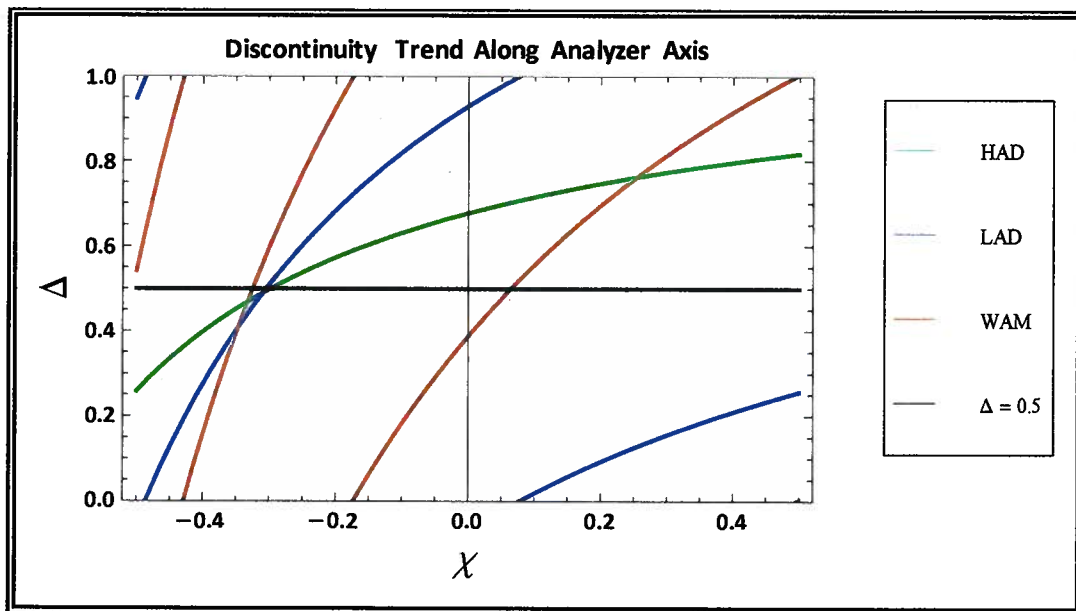


Figure 3.1. Functional form of Δ based on the previous derivations in this chapter. The discontinuity positions in table 3.1 are visible as curves passing through 0.5 for slit correction data with an even number of iso-angle contours, or when reaching the value of 1 if there are an even number of iso-angle contours in the slit correction data.

The angular acceptance of the WAM, LAD, and HAD lens modes of the Phoibos 150 are specified by the manufacturer and are given in table 3.1. The ideal solid angle of analyzer acceptance can be determined from equation 3.1 with $y = 0$ and $L_A = 40\text{mm}$ as specified by SPECS. From this the value of D can be determined, as well as σ , for which results are also given in table 3.1. Table 3.1 and figure 3.1 provide specific information for the symmetric

IAC appearance as a function of x .

Deviation of Point Source Position from the Optical axis

Returning to the general equation 3.3, the results of the previous section can be expanded to address the SCD image symmetry and the observable effect of moving the point source along the optical axis in the situation where the ADP are arbitrary. Two special cases will be examined, for which one of the ADP is fixed at the value of the NCIACA, and the other is varied. This will be done for both odd and even total IAC. Afterward a general case will be derived in which both ADP are variable. The focus in this work is in looking for values of the ADP where both n_1^* and n_2^* change at the same time when varying the point source position along the focal point, as this gives a clear signature in the SCD. This section will clearly elucidate the best method for the experimentalist to position the point source and slit array in order to approach the ideal positions of the NCIACA.

In the case of variable y with fixed σ , the even and odd cases will be similar to the last section, except that Δ can be considered to take on an effective offset of size $\frac{L_S}{d L_A} y$. This can be seen in the modified equations for the effective number of IAC,

$$\begin{array}{cc}
 \text{Even \# of IAC} & \text{Odd \# of IAC} \\
 n_{\pm}^* = \left(n + \text{Floor} \left[\Delta \pm \frac{L_S}{d L_A} y \pm \frac{1}{2} \right] \mp \frac{1}{2} \right) & n_{\pm}^* = \left(n + \text{Floor} \left[\Delta \pm \frac{L_S}{d L_A} y \right] \right)
 \end{array}$$

There will be an integer jump in n_{\pm}^* as the argument of the floor function approaches one. However, the jump does not occur at the same value of Δ for both n_+^* and n_-^* . This is because of the effective offset introduced by y . Generally, change in the position x will not give a symmetric set of IAC entering or leaving the SCD image on either side because of this offset, though it is interesting to note that for special values of y the symmetric IAC entering with x situation would occur. This is the case where,

$$\begin{array}{cc}
 \text{Even \# of IAC} & \text{Odd \# of IAC} \\
 \Delta + \frac{L_S}{d L_A} y + \frac{1}{2} = i & \Delta + \frac{L_S}{d L_A} y = i
 \end{array}$$

$$\Delta - \frac{L_S}{d L_A} y - \frac{1}{2} = j \qquad \Delta - \frac{L_S}{d L_A} y = j$$

with i and j integers. Reducing the equations by eliminating Δ gives,

$$\begin{array}{ll} \text{Even \# of IAC} & \text{Odd \# of IAC} \\ y = \frac{(i-j-1) d L_A}{2 L_S} & y = \frac{(i-j) d L_A}{2 L_S} \end{array}$$

The symmetric IAC jump is effectively a signature of these special values of y when σ is assumed to be the NCIACA value.

The next situation has variable σ with fixed y . The equations for the number of IAC becomes,

$$n_{\pm}^* = \left(n + \text{Floor} \left[\Delta \pm \frac{\sigma}{d} \right] \mp \frac{\sigma}{d} \right)$$

This holds for the even and odd case, though in the even case $\sigma = 1/2$ is the NCIACA value, while it is $\sigma = 0$ for the odd case. Here again there is an offset parameter in the floor function, and we can go straight to the symmetric IAC change condition,

$$\sigma = \frac{(i-j)}{2} d$$

In this case, however, σ is only used within the range $-d/2 \leq \sigma \leq d/2$, so that the difference in i and j is no more than one in magnitude. With this result, the symmetric IAC change is seen to occur with change in x when,

$$\sigma = -\frac{d}{2}, 0, \frac{d}{2}$$

with y is assumed to be the NCIACA value. This is very useful, because if the point source is at the focal point of the analyzer, then the symmetric IAC change condition requires that the slit-array offset ADP is equal to the NCIACA value, enforcing the validity of this approximation once the focal point has been reached.

Finally, we can expand this treatment to be useful in the general case with both ADP parameters variable. Returning to equation 3.2 and proceeding in the same way as in the two special cases gives the result and representation with unitless parameters,

$$\frac{(i-j)}{2} = \left(\frac{L_S}{L_A}\right) \cdot \left(\frac{y}{d}\right) + \left(\frac{\sigma}{d}\right) \rightarrow \rho \bar{y} + \bar{\sigma}$$

$$\rho \equiv \frac{L_S}{L_A}, \bar{y} \equiv \frac{y}{d}, \bar{\sigma} \equiv \frac{\sigma}{d}$$

In the general case the symmetric IAC change is seen to occur for special cases of the combination of the two ADP, in such a way that they combine to form a half-integer. If we use m as an integer, we can write this condition as,

$$\bar{y} = \frac{1}{\rho} \left(\frac{m}{2} - \bar{\sigma} \right) \quad (3.4)$$

This does not directly enable the experimentalist to set the ADP to the NCIACA values when the symmetric IAC change SCD signature is obtained, because at best there is only knowledge of the interrelation of the ADP. Unless one ADP is known, they are both unknown. However, there is more information available that can be obtained from spatially resolved lens modes.

Since some general knowledge of the position of the focal point comes from the ARPES chamber geometry, it is possible to roughly know where the focal point is located, and from this starting point the spatially resolved analyzer lens modes can be used to minimize the values of y for the electron emission point source. One procedure that will significantly increase the ADP proximity to ideal values is for the minimization of y to be followed by the modification of σ to achieve the symmetric IAC change condition. Equation 3.4 can then be used to get the maximum size of error in y . Since $-1/2 \leq \bar{\sigma} \leq 1/2$, the largest deviation in y from the focal point can be determined to be $(d/2\rho)$, which is,

$$\delta y = \frac{d}{2} \left(\frac{L_A + x}{L_S + x} \right) \cong \frac{d}{2} \frac{L_A}{L_S} + \frac{(L_S - L_A)}{L_S^2} \delta x$$

Before the final ARPES experiment, the value of x is set to zero to make θ the

appropriate value for the analyzer lens mode, and in this way the NCIACA can be closely achieved in practice.

Calculation of Errors in the Nearest Central Iso-Angle Contour Approximation

In applying the NCIACA, there is the fact that the positions in the real experiment are not exactly at $y = \sigma = 0$, and the level of approximation involved in this assumption must be evaluated in order to determine its validity. There are four important quantities that we obtain from the formalism developed in this chapter.

- i. Angle between extreme IAC
- ii. Position of the zero of detector angle
- iii. Position of the analyzer focal point
- iv. Effect of z-axis offset

In this section, the error in these quantities will be determined in all parameter regimes that are accessed in an ARPES experiment intended to determine the values of these quantities. Error analysis will be done with the method of propagation of random independent uncertainties⁵.

i. Angle Between Extreme Iso-Angle Contours

The angle between extreme IAC is already known generally from equation 3.2. There are distinct regions of this equation that require separate expansions for errors, because of the floor function. Within each region, the floor function can be considered a constant with no contribution to the error except when the uncertainty of the argument of the floor function is large enough to allow an adjacent region to be accessed by the distribution of random error. In the case where $y \approx 0$ and $\sigma \approx 0$, then we can consider $n_+ = n_- = n$ to be constant. Since n is considered to be a constant, the variable y does not play a role in the calculation, and only the offset of the slit array relative to the point source contributes.

Expanding 3.2 about the NCIACA value of $\sigma = 0$ gives,

⁵ Taylor, J. An Introduction to Error Analysis. University Science Books, California, 1997.

$$\theta' \approx 2 \tan^{-1} \left[\frac{n d}{L_S} \right] - \frac{2(n d L_S) \sigma^2}{(n^2 d^2 + L_S^2)^2} + \mathcal{O}(\sigma^4); \sigma \cong 0$$

$$(\delta\theta'(\sigma \rightarrow 0))^2 \cong \left(\frac{\partial\theta'}{\partial d} \delta d \right)^2 + \left(\frac{\partial\theta'}{\partial L_S} \delta L_S \right)^2 + \left(\frac{2(n d L_S) (\delta\sigma)^2}{(n^2 d^2 + L_S^2)^2} \right)^2$$

The derivatives of θ' with respect to d and L_S are:

$$\left. \frac{\partial\theta'}{\partial d} \right|_{\sigma=0} = \frac{2 L_S n}{L_S^2 + (nd)^2}$$

$$\left. \frac{\partial\theta'}{\partial L_S} \right|_{\sigma=0} = \frac{-2nd}{L_S^2 + (nd)^2}$$

If an even number of IAC is present, then the situation is different, because of the difference in n_+ and n_- . However, the error analysis ends up being identical with the simple replacement of $n \rightarrow n + 1/2$ and with σ being taken to describe deviation from the point $\sigma = d/2$ that we had before.

ii. Zero of Detector Angle

The location of the zero of detector angle will be somewhat different than the location stated in the NCIACA as long as y and σ are nonzero. Knowing the zero of detector angle is equivalent to knowing the true value of the electron emission angle at the location assumed to be the detector angle zero in the NCIACA.

The exact value of the electron emission angle deviation from normal incidence to the analyzer entrance is related to the IAC nearest the detector angle zero from,

$$\Phi = \tan^{-1} \left[\frac{\sigma}{L_S + x} \right]$$

If we take the uncertainty in Φ to be the measure of the precision of the angle at which the NCIACA central angle value is known, we have,

$$(\delta\Phi)^2 \cong \left(\frac{\delta\sigma}{(L_S + x) \left(1 + \frac{\sigma^2}{(L_S + x)^2}\right)} \right)^2 + \left(\frac{\sigma}{(L_S + x)^2 + \sigma^2} \right)^2 (\delta L_S^2 + \delta x^2) \quad (3.5)$$

If there are an odd number of IAC in the SCD image, then σ is expected to be zero, in which case equation 3.5 reduces to,

$$\delta\Phi = \frac{\delta\sigma}{L_S + x}$$

, to first order in σ . In the even case, the uncertainty becomes to first order,

$$(\delta\Phi)^2 \cong \left(\frac{\delta\sigma}{(L_S + x) \left(1 + \frac{(d/2)^2}{(L_S + x)^2}\right)} \right)^2 + \left(\frac{(d/2)}{(L_S + x)^2 + (d/2)^2} \right)^2 (\delta L_S^2 + \delta x^2)$$

iii. Focal Point

From the value of Δ for which n_{\pm}^* has a discontinuity, the analyzer focal point position x can be determined from the SCD. From equation 3.3 we can see that there will be a discontinuity when,

$$\Delta \pm \frac{y(L_S + x)}{d(L_A + x)} \pm \frac{\sigma}{d} = i$$

for integer i . This can be expanded as,

$$\begin{aligned} \frac{(L_S + x)D}{2d(L_A + x)} \pm \frac{y(L_S + x)}{d(L_A + x)} \pm \frac{\sigma}{d} &= i + \text{Floor} \left[\frac{(L_S + x)D}{2d(L_A + x)} \right] \\ &\rightarrow \frac{(L_S + x)D}{2d(L_A + x)} \pm \frac{y(L_S + x)}{d(L_A + x)} \pm \frac{\sigma}{d} = i' \end{aligned} \quad (3.6)$$

for the new integer i' . The uncertainty in this quantity is related to the uncertainty in the position x , which is what we are interested in. We can rearrange this to get an equation for x :

$$x_{\pm} = \frac{\left(L_S \frac{D}{2d} - L_A i' \right) \pm \left(L_S \frac{y}{d} + L_A \frac{\sigma}{d} \right)}{\left(i' - \frac{D}{2d} \right) \mp \left(\frac{\sigma}{d} + \frac{y}{d} \right)}$$

The uncertainty in x can be calculated directly from this equation, but this will lead to an equation that has y and σ as parameters that must be known to evaluate the uncertainty. These parameters are not precisely known in ARPES, which is the entire basis of necessity for the NCIACA. Since, the value of x for the minus and plus branches are equal only when both y and σ are zero, we can in practice find a regime where the symmetric IAC change occurs, and so at first approximation we can take y and σ as their NCIACA values and examine the effect of uncertainty in y , σ , and the other parameters.

First, we can redefine D in terms of solid angle of acceptance, ψ , in the analyzer lens mode.

$$D = 2 L_A \tan \left[\frac{\psi}{2} \right]$$

The uncertainty becomes,

$$\begin{aligned} (\delta x_{\pm})^2 \cong & \left(\frac{L_A \tan \left[\frac{\psi}{2} \right]}{d i' \mp \sigma - L_A \tan \left[\frac{\psi}{2} \right]} \delta L_S \right)^2 + \left(\frac{(\sigma \mp d i') (\sigma \pm L_S \tan \left[\frac{\psi}{2} \right] \mp d i')}{(\sigma \pm L_A \tan \left[\frac{\psi}{2} \right] \mp d i')^2} \delta L_A \right)^2 \\ & + \left(\frac{i' L_A (L_A - L_S) \tan \left[\frac{\psi}{2} \right]}{(\sigma \pm L_A \tan \left[\frac{\psi}{2} \right] \mp d i')^2} \delta d \right)^2 + \left(\frac{(\sigma \mp d i') (L_A - L_S)}{(\sigma \pm L_A \tan \left[\frac{\psi}{2} \right] \mp d i')^2} \delta y \right)^2 \\ & + \left(\frac{L_A (L_A - L_S) \tan \left[\frac{\psi}{2} \right]}{(\sigma \pm L_A \tan \left[\frac{\psi}{2} \right] \mp d i')^2} \delta \sigma \right)^2 \quad (3.7) \end{aligned}$$

Here, σ is zero when there are an odd number of IAC, and $\sigma = d/2$ when the number of IAC is even. The parameters ψ and i' are taken to be constants that do not have uncertainty, because the first one is given by the analyzer manufacturer and the second is required to be an exact integer quantity. The value of i' can be taken to be the value from equation 3.6 when $i = 0$, since this is the case for y and σ zero and the ARPES experiment is done in such way as to be near enough to this situation that the values of y and σ balance the nonzero value of Δ and remain in the $i = 0$ regime. If y and σ are further from zero, it is

possible that i is nonzero, and additionally the approximate error calculation done here would not be valid for that situation.

The standard deviation δy is an important contributor in the uncertainty δx , because δy is related to the precision of the calculated focal point relative to the position of discontinuity that leads to the symmetric IAC change. This is the only error calculation in this work that involves δy . In the other error propagation calculations, as long as y is close to zero in the ARPES experiment, for instance by minimizing its value through a spatial analyzer mode, then it does not contribute significantly to the errors here.

iv. Z-axis

The offset of the point source in the z-direction has not yet been mentioned. The effect of the illumination of a point that is offset from the optical axis in the z-direction will only effect the uncertainty in the other angle, ϕ . It will only contribute to the uncertainty in the detector angle by increasing uncertainty in L_S and L_A , unless some intrinsic function of the electron lens system becomes important. This last effect will not be considered in this work, as we will assume that the offset is small enough that this is negligible. The effect on L_S and L_A can be readily quantified as,

$$L_S = \sqrt{L_{S0}^2 + z^2}$$

$$L_A = \sqrt{L_{A0}^2 + z^2}$$

The uncertainty can be modified to explicitly take this into account, but for the purposes of this project it will only be necessary to make δL_S and δL_A large enough to reasonably accountable for this additional uncertainty.

Chapter 4 Image Warping

To proceed further, clarification of the methods of image warping and necessarily the reconstruction of discretely sampled data will be necessary. The starting point in data reconstruction is the theory of Shannon, which proves perfect reconstruction is possible. Unfortunately, application of this theory is inefficient or unpractical due to the necessity of Sinc weighted sums over many points and the requirement of a band-limited signal⁶. It has been shown, however, that by loosening the requirement for orthogonality in the reconstruction basis functions, a basis of functions with much greater flexibility and computational efficiency can be constructed, which will in practice asymptotically approach the perfect reconstruction of Shannon, without the precondition of a band-limited signal⁷. This is the basis of B-spline functions, which underlie polynomial splines and are known to be compactly supported for greatest efficiency⁸.

There are two different approaches to image warping - "forward" interpolation and "reverse" interpolation. The definition of forward and reverse refers to the direction of mapping between the original and final image. The forward case is where a mapping is applied to integer pixel coordinates in the original image, in order to determine final coordinates at which the intensity at the original coordinate is distributed in the final image. The mapping function will output a non-integer coordinate in the final image, and some way of assigning the intensity to one or more integer coordinate pixels in the final image must be decided.

The alternative approach is known as reverse interpolation, because it reverses the mapping and applies it to integer final image coordinates to obtain non-integer positions at which the intensity must be interpolated between the existing integer points in the raw ARPES data. The interpolated intensity is then assigned to the final image coordinate. The mapping used in reverse interpolation is the inverse of the one used in forward interpolation and implicit in this discussion is the invertibility of the mapping function, though it should be

⁶ Unser M. 2000. Sampling – 50 Years After Shannon. *Proceedings of the IEEE*, 88(4):569-587.

⁷ Unser M, Aldroubi A, Eden M. 1992. Polynomial Spline Signal Approximations: Filter Design and Asymptotic Equivalence with Shannon's Sampling Theorem. *IEEE Transactions on Information Theory*, 38(1):95-103.

⁸ Unser, M. 1999. Splines: A Perfect Fit for Signal/Image Processing. *IEEE Signal Processing Magazine*, 16(6):22-38.

fairly clear from the implementation in this work that this will be the case. The satisfaction of the invertibility condition means that the situation for the reverse procedure is analogous to the forward one, though it is simpler to understand the effect of the detailed interpolation scheme in the reverse case because it is a straightforward interpolation of the raw data as opposed to redistribution in the final image⁹.

The computational implementation of the reverse mapping involves interpolation of the intensity data at non-integer coordinates. There are many accurate and efficient interpolation techniques available for this purpose. In the computer program developed and used in this work, linear splines were used to reconstruct the intensity function and produced favorable results. The accuracies at points that are interpolated from the original data is not easily determined, however the basic reliability of the methods used in this project for sampled-data reconstruction is well known¹⁰.

It should be mentioned that there is an additional approach that makes use of non-uniform data, that is essentially a group of data that is not in the form of an array, but instead just a list of points and their values. This is achieved by applying the forward mapping function to the raw ARPES image and recording the non-integer positions along with their accompanying intensity. At first glance this is very similar to forward interpolation, but in truth the non-uniform method is more general since it does not directly involve any interpolation. Actual use of the non-uniform output for plotting or any type of analysis requires fairly advanced interpolation of the non-uniform data^{11,12}. This method is in the end much more complicated than the forward and reverse methods, due to the interpolation necessary for analysis. While the non-uniform method exceeds the scope of this work, it does offer an interesting way to avoid interpolation until the point where a specific analysis task is undertaken, and may lead to interpolations that have more elucidating physical interpretation.

⁹ Wolberg G. 1996. Recent Advances in Image Morphing. Proc. Computer Graphics Internat., 64-71.

¹⁰ Thevenaz P, Blu T, Unser M. "Image Interpolation and Resampling." Handbook of Medical Image Processing. New York: Academic, 2000 ,chapter 25.

¹¹ Ruprecht D, Mueller H. 1995. Image Warping with Scattered Data Interpolation. IEEE Computer Graphics and Applications, 15(2):37-43.

¹² Amidror I. 2002. Scattered Data Interpolation Methods for Electronic Imaging Systems. Journal of Electronic Imaging, 11(2):157-176.

Procedure of Finding Peak Positions in Slit Correction Data

Once a satisfactory SCD image is obtained from the experimental apparatus, the position of the iso-angle contours can be determined. This was done by finding the peak position of an EDC in the signal that forms the contours, since no a priori line shape is expected in the electron emission from a sample of electron scattering from the tungsten wire point source.

In theory one needs to simply fit all the peaks for every column of the image, though this is both time intensive and in some cases impossible due to regions of low intensity of nearly overlapping lines, for which the location of peak positions is indeterminable from the standpoint of peak finding algorithms that are not excessively complicated or time intensive. There are multiple solutions to this type of problem, and in this work a method has been developed that utilizes a curve of best fit algorithm to obtain a functional relationship for the peak positions from algorithms that locate the peaks for a specified number of columns of the SCD image.

The peak position changes as a function of energy, so that fitting of the peak position versus energy is possible with any function which accurately represents the contour shape. In low angular dispersion (LAD) mode, this is usually only a linear function, since nonlinear distortion is minimal in this setting. Analyzer modes that attempt to capture a larger energy range have intrinsically higher angular distortion, so it was necessary to use a square root function in the case of the wide angular mode (WAM) to fit the peak positions that form the contour.

The peak finding algorithm used in this work is a sigma optimization applied to the “peaks” algorithm and its dependencies, provided by John Johnson¹³. The “peaks” algorithm relies on the routine “robust_sigma”, provided by the NASA Goddard Space Flight Center IDL Library¹⁴. In the peaks algorithm, all of the peaks are located via simple search for local maxima in a vector list. Next, robust_sigma is applied to the peaks to determine their standard deviation. The variable NSIG is supplied to the algorithm, and it returns the peak positions for peaks that are NSIG above the standard deviation of all of the peaks that were found¹³.

In this work, “peaks” has been modified to incrementally adjust the value of NSIG until

¹³ <http://astro.berkeley.edu/~johnjohn/idl.html#PEAKS>

¹⁴ <http://idlastro.gsfc.nasa.gov/cgi-bin/idllibsrch?keyword=robust+sigma>

the number of peak positions it returns is equal to the number of IAC lines that the user has specified to be present in the SCD. NSIG is increased or decreased until the correct number of peaks is returned, and these peaks are then guaranteed to be the peaks with the highest statistical significance and must be the IAC positions. There are some exceptions, notably when the finite peak width of the IAC causes two peaks to merge, in which case only a single peak is detected. If there is statistical noise that could cause certain peaks to appear to the routine as very closely spaced double-peaks, then a smooth operation can be applied to the vector list with user-defined smooth length in order to eliminate spurious double-peaks.

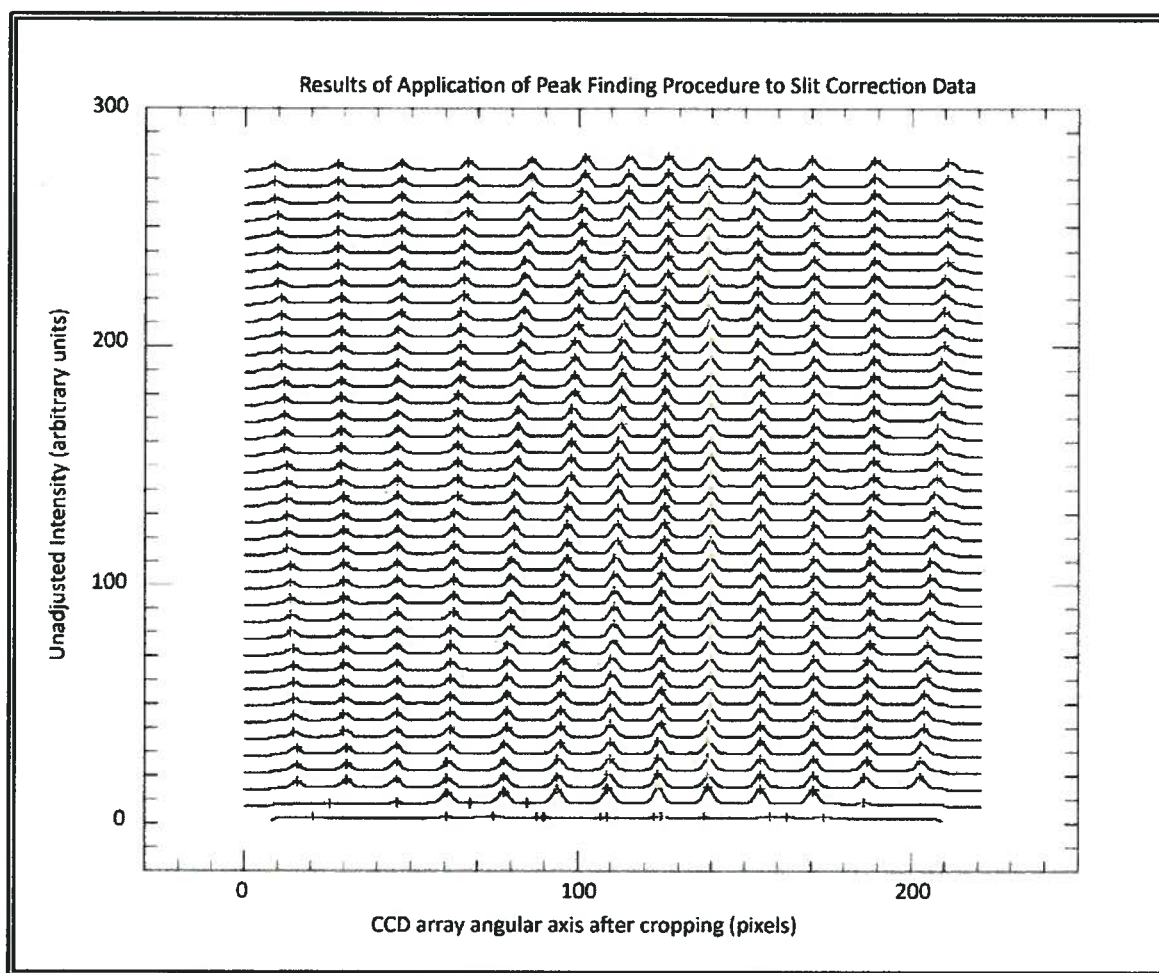


Figure 4.1. The application of peak finding to data similar to figure 2.2 shows favorable results. Positions of each color type are found by the peak fitting routine to belong to the same iso-angle contour. There is difficulty in finding the positions at the edges of the data set, where the peaks are not well defined, and can be seen near the bottom of the figure.

Peak position can be determined on as many columns as desired for high accuracy, as shown in figure 4.1. In finding the peak positions, one encounters difficulty at the edges of the data because of the rapidly diminishing peak heights. To resolve this issue, a fit function applied to the easily found peak positions can be used to extrapolate to regions where finding the peak positions is difficult. This avoids the need to crop regions of data that have angular distortion reasonably well characterized by the analytic continuation of the peak position fit function.

Final Positions to Construct the Discreet Coordinate Mapping Function

The mapping function can be defined to give the position of the final coordinates in terms of the original coordinates, where original is in reference to the raw data that is directly output from the ARPES experiment, that does not possess image parameter orthogonality. The final image is taken as a reference to the image with IPO that is the final result of the distortion correction. From the discussion thus far it is clear that the mapping is needed to connect the original position of IAC as found by the peak fitting process in the last section to the final positions that are defined in a coordinate space with IPO. In essence, the mapping is orthogonalizing the angle axis to the kinetic energy axis in the DFED situation.

The previous section outlined the procedure by which the original positions are found, and in order to create the mapping the final positions are required. These positions are not measured coordinates, but rather theoretically derived values based on measured quantities, and some explanation of the concept behind this construction is required. The theory behind the NCIACA has already been derived in detail, and the fundamental equations here follow in the same way, although here we can use the iterator i to describe the position of each IAC. There are two equations that give the final positions on either side of the NCIACA central position.

$$x'_i{}^\pm = \pm \gamma \tan^{-1} \left[\frac{i d \mp \sigma}{L_S} \right]; \quad 0 \leq i \leq n_\pm \quad (4.1)$$

The value of σ is $d/2$ for the case where there are an even number of IAC, and σ is zero for the odd case. The final positions can be seen to be constructed from the angle of the IAC relative to the NCIACA central position multiplied by the pixel per angle ratio, γ . Any constant added to equation 4.1 is arbitrary since it will not affect any physical quantities in the data, and so it has been assigned to zero for simplicity.

Given that the original positions are already known, the task at hand is to assign the peak positions to the plus or minus branch of the final positions, and give the original positions a one to one correspondence with the final positions calculated from equation 4.1. By this process a discreet mapping function is created that couples each of the original peak positions with a position in the final image such that the final coordinates obeys the IPO requirement.

Fitting of the Mapping Function

With the original positions and final positions, all of the information is present for the map to be established. This is of the form:

$$m_i = [x_i, x'_i], \text{ for } 1 \leq i \leq N_{peaks}$$

N_{peaks} is the number of iso-angle countours in the SCD image. The important limitation in this description of the map is that we only have N_{peaks} points that are well determined. For positions of the original image that do not correspond to any x_i , there is no information available on the true nature of the mapping. For this reason, there is no choice but to analytically continue the function between these points with an interpolation. The methods used for this interpolation and for the intensity data proceed in the same way discussed in the first section of the chapter.

The Conservation of Spectral Weight

The issue of spectral weight conservation is an important one for ARPES data, because of the physical significance of the total spectral weight and its relation to the density of states. In the attempt at reverse mapping with spectral weight conservation, it must be understood that there is no exact solution and some level of approximation is necessary. This is due in part to the fact that we do not know the exact value of the mapping function at all points, and we do not have knowledge of the data at positions that do not correspond to a single pixel on the ccd array. It is necessary to apply an equation of best fit to the mapping function points obtained from IAC, and after an analytic fit is obtained, the properties of the mapping that describe spectral weight conservation can be very accurately determined from the mapping

function. The accuracy of spectral weight conservation is increased by the decrease in inter-point interval of the fitted mapping function, and is therefore dependent on the precision of the mapping function.

The conservation of image intensity after warping is described by change of variables and the Jacobian. In the case of one dimensional mapping with a continuous variable we can write the Integral equation¹⁵:

$$\int_a^b I(x) dx = \int_{x(a)}^{x(b)} I(x'(s)) \frac{dx'(s)}{ds} ds$$

The function $x'(x)$ is the forward map and $x(x')$ is the reverse map. Two things are evident from this equation. First, the intensity function has changed from $\{I(x): a \leq x \leq b\}$ to $\{I(x'(s)): x(a) \leq s \leq x(b)\}$. Secondly, the integral of the intensity function over the corresponding regions before and after the mapping is not the same, and in order to achieve equality a weight function defined by the derivative of the forward mapping, dx'/dx , must be introduced under the integral.

If the conservation of intensity was the only issue involved, the problem would have already been solved. By multiplying the distortion correction data by the derivative of the forward mapping, the integral of the final image would be as close as possible to the integral of the original image, likely differing only slightly due to some numerical errors in the calculation of the derivative. In the case of reverse interpolation, this would lead to the final image given by,

$$I'_{i,j} \rightarrow I'_j(i) = I_j(x_j(x'_{i,j})) \frac{dx_j(x'_{i,j})}{dx'_{i,j}} \quad (4.2)$$

In this case the discreet nature of the coordinates has been directly utilized. The notation of $I'_{i,j}$ for the final image pixel coordinates is equivalent to $I'_j(i)$. The notation $I_j(x_j(x'_{i,j}))$ represents the interpolation of the intensity of the original image column j at positions given by reverse map x_j evaluated at the integer final image coordinates $x'_{i,j}$. The last term is the Jacobian, which is the derivative of the reverse map evaluated at the final

¹⁵ Lax, P. D. 1999. Change of Variable in Multiple Integrals. Amer. Math. Monthly 106: 497-501.

image coordinates. We can show intensity conservation in this equation by taking the continuous limit,

$$\sum_i I'_j(i) = \sum_i I_j(x_j(x'_{i,j})) \frac{dx_j(x'_{i,j})}{dx'_{i,j}}$$

$$\rightarrow \int I'_j(s) ds = \int I_j(x_j(t)) \frac{dx_j(t)}{dt} dt ; \lim x'_{i,j} \rightarrow t$$

However, while this is a starting point, the reason this is not the final answer to spectral weight conservation is that we require the preservation of more than just the integrated intensity. There are two primary and fundamental types of information that can be extracted from ARPES data, and type one is integrated quantities that involve the averaging or summation of ARPES data. Type two information has nothing to do with integration, and instead focuses on the location of features that are indicated by peak positions, local maxima, constant intensity profiles, and any feature related to a specific or relative intensity value, such as half-width-half-maximum analysis to determine peak width.

The problem with multiplying the entire data set by the Jacobian function is that it is not clear to what extent this method will preserve both types of information, because the function,

$$I'_{i,j} = I_j(x_j(x'_{i,j})) \quad (4.3)$$

The distortion correction without the Jacobian, already preserves the intensity versus angle and energy information that is the basis for type two information. However, the equation 4.3 does not preserve type one information, while equation 4.2 does.

It is clear that if type one information is not preserved, then the physical picture of ARPES intensity in relation to a measure of the electron density of states is destroyed, which is a serious problem for physically relevant analysis of the distortion corrected ARPES images. Some way of reconciling the two pictures is necessary, but the impasse in doing so centers around the fact that we do not have functional equation for spectral weight conservation, only an integral equation¹⁶.

Since this issue may be of relevance later, I have chosen to perform the distortion correction in such a way that the result has two layers of data. One is the pure distortion

¹⁶ See appendix B for more information.

correction as given by equation 4.3, without the Jacobian. The second layer to the data array is the Jacobian. In this way, no information is lost. The reconciliation of the two data layers via a functional relationship for the conservation of spectral weight will necessarily be the subject of future work.

Extensions in Two Dimensions

While this work does not implement a two dimensional distortion correction due to DFED as a starting point, it is interesting to note that the two dimensional case can be separated into two one dimensional cases if desired. A direct 2D distortion correction is certainly possible, and it would proceed in the same manner as already described for the 1D case, if we extend all univariate functions to functions of both angle and energy. A two dimensional Jacobian can be derived from the now 2D mapping function, whereas before we had a list of independent 1D mapping functions. While this is a valid method, the presence of two calibration images for both iso-angle and IEC allows an alternative approach.

In the case where we begin with the iso-energy contour image as discussed, it has been shown that a reverse mapping distortion correction can be constructed from the information in the raw ccd data. If that correction is applied to the second, iso-angle calibration image, then that calibration image is equivalent to the iso-angle calibration image in the DFED case. Proceeding exactly as detailed in the previous section, a second reverse mapping distortion correction can then be constructed. Applying these two mappings in the same order to the data, will result in data corrected in two dimensions. While this is not implemented in this work due to the simplicity of DFED in the SPECS Phoibos 150 Analyzer, this discussion illustrates the usefulness of the 1D distortion correction and the simplicity of generalizing it to arbitrarily higher dimensions by utilizing intermediate mappings of the iso-parameter calibration images.

Chapter 5 Experimental Procedure for Determining the Focal Point

The process by which the ideal positions x , y , and σ can be found has been outlined and its relevance explained within the context of a theoretical calculation. It is useful at this point to elucidate this discussion with an example of the application of these principles on the UBC ARPES system. In this experiment the vertical tungsten filament was used as the point electron emission point source, with the electron source as . The position of the point source was modified along the x and y directions in concurrence with the existing definitions of these parameters, and the electron beam was steered in order to maintain illumination of the tungsten wire. The electron source was set to an emission current of $10\mu\text{A}$.

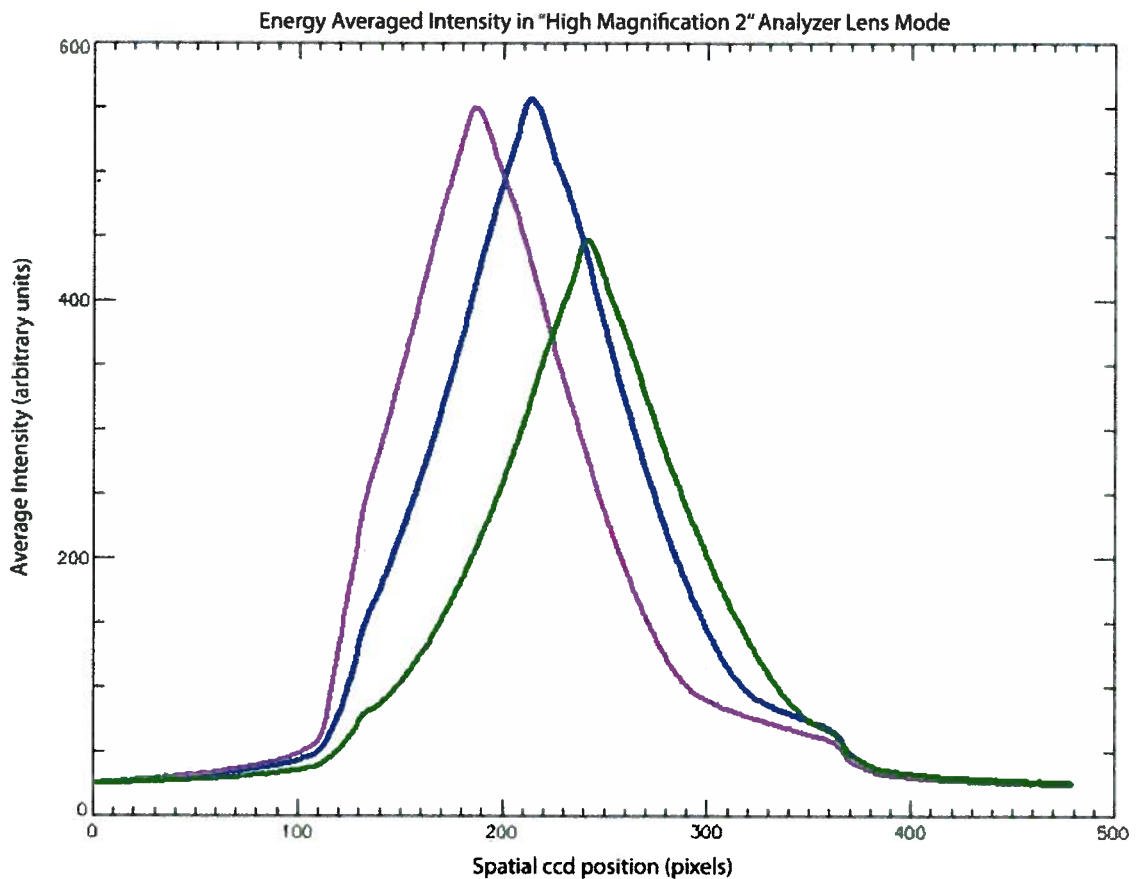


Figure 5.1. The energy averaged photoemission signal from the tungsten wire as y is changed. The green curve is peaked at the approximate center of the ccd camera.

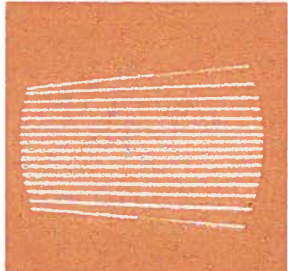
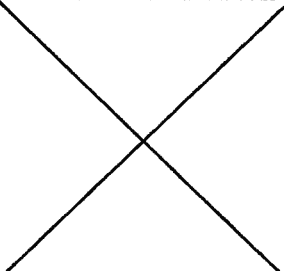

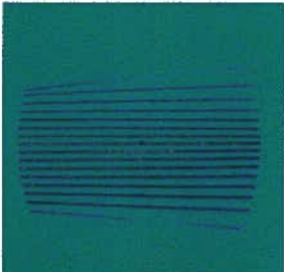




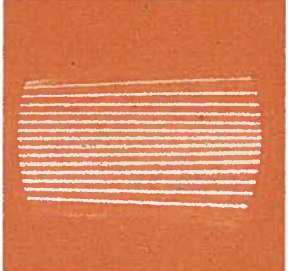

Position	Detector Image	Image Difference From X=-0.5
Cryostat X = -0.5 mm		
Cryostat X = -1 mm		
Cryostat X = -1.5 mm		
Cryostat X = -2 mm		
Cryostat X = -2.5 mm		

Figure 5.2. Uncorrected ARPES images versus cryostat position.

First the high magnification analyzer mode was chosen as a suitable spatially-resolved lens mode in order to set the y position to a value that indicated the point source was in the center of the image. This condition was met when the central peak of the detector image was centered around pixel 240 of 480 on the ccd camera, as shown in figure 5.1. The blue and purple curve are included only to show the signature of the point source position y being far from the ideal central value. The green curve illustrates a well-centered position that is close to the NCIACA situation.

The next component of the procedure involved moving x to a position where either an even or odd IAC situation allowed the adjustment of the slit array position σ to achieve symmetric IAC change on either side of the detector image. Once this was done, x was varied again in either direction to assess the range of x for which symmetric line change was observable, and the results appear in figure 5.2. Assessment of the range of x was necessary because of finite line thickness and small variation in the effective analyzer acceptance solid angle with energy caused only partial line removal at the sides of the detector image to be observable at any given value of x .

From the results of this procedure, the symmetric iso-angle contour change appears to occur primarily between cryostat x position of -0.5 mm and -2.5mm. This is a large range, and since the value cannot be specifically found in this range, this represents the largest contribution to the error of the focal point determination in an experimental setting. Proceeding by use of the calculations of table 3.1 result in a symmetric line change for an even number of IAC at $\chi=0.0647$. Taking the manufacturer specification of $L_A=40$ mm, we have the position of the point source to be $x=2.59$ mm relative to the analyzer focal point at $x=0$. A discrepancy between the cryostat position and point source position is found to lie in their definition of positive axis as opposite to one another. Therefore, to obtain the focal point in the cryostat coordinate we add the negative cryostat position to the positive point source position to find that the focal point is at cryostat position $x = 1.09\text{mm} \pm 1.00$ mm.

Comparing with the calculated error of equation 3.7, in choosing $\psi = 13$ degrees, $d=1$ mm, $L_A=40$ mm, $L_S=32$ mm, $\sigma = 0.5$ mm, $y=0$, $\delta L_A = \delta L_S = 0.5$ mm, $\delta\sigma=0.1$ mm, and noting that for the approximate values here the minus branch should be taken with $i'=7$ or the plus branch with $i'=8$, to get $\delta x=1.07$ mm. The experimental accuracy agrees very well with the calculated uncertainty for these reasonable parameter choices.

Post Distortion Correction Detector Angle Axis

The final determination of the detector angle axis is important for the finalization of the initial stages of warping the raw ARPES images into the more useful form with IPO. When this is done, a single-shot ARPES image will contain a three dimensional function of intensity over the variables of detector angle and kinetic energy, and the benefit of the distortion correction stage will be that this function is now described in an orthogonal coordinate system. In order to proceed with analysis, however, it is fundamental to quantify the angle axis. Detector angle is not known a priori, much unlike the kinetic energy axis that is given by analyzer kinetic energy and pass energy that are fixed settings in an experiment and specified beforehand. Without the angle axis, clearly there is no possibility of quantifying the angular information accompanying intensity features. In order to determine this axis, several pieces of information already processed in the distortion correction phase will be used to get the slope and offset parameters for a line quantifying the detector angle axis.

The mapping function of the distortion correction was constructed with the peak positions of IAC in the data of the initial calibration experiment, as well as the final locations determined for these points. The definition of final locations requires the use of a slope-like parameter γ in pixels per angle, which is essentially arbitrary but can conveniently be set to the median separation of extreme IAC in the calibration divided by the angle calculated between these positions in the framework of the NCIACA. Despite what value of γ is chosen, it remains that the definition of this parameter has the effect of defining the distortion correction mapping to direct the raw data intensity to a location on a linear angle axis with slope of γ . Therefore the choice of γ that was involved in the distortion correction has already defined one of the two parameters that quantify the angle axis.

The final parameter of the detector angle axis is an offset that can be considered to place the zero of the axis at the appropriate position in the final image. From the NCIACA, we have approximately determined the central position in the case of either an even or odd number of visible IAC in the calibration experiment, and this information has been incorporated into the final positions of the coordinate mapping function of the distortion correction. In this process, the final IPO image has the contour that is the locus of all NCIACA zero-angle positions as a straight line perpendicular to the detector angle axis. The location of the zero-angle line must be determined by applying the mapping function to the original zero-angle positions and finding where they occur in the final image. The position

will in general not be an integer pixel coordinate in the final image, though a detector angle offset can be determined to make the detector angle axis zero at the non-integer position.

Once both the slope, γ , and offset, b , are known, it is a relatively simple matter to construct and evaluate the angle axis at final image coordinate x . The axis can be described by the equation,

$$\Theta_{\text{detector angle}} = \frac{x}{\gamma} + b$$

where the parameters γ and b are specified so that $\Theta_{\text{detector angle}}$ has units of degrees. The inverse of γ is used in the equation because it is defined in pixels per angle and its inverse can be multiplied by the pixel coordinate x to return a value in degrees. This is equivalent to redefining a slope parameter in units of angle per pixel, though its value would be identical to the inverse of γ . Finally, the detector angle axis is created as a vector quantity by evaluating the equation at each integer coordinate in the final image.

At the end of the process described in this section, the angle value simultaneous with each intensity pixel in the final, IPO image is completely described. This was accomplished with knowledge of the slope and offset parameter of the detector angle, which are related to the distortion correction and the coordinate mapping therein. While the slope parameter is not directly connected to any physical quantity, this is not so for the offset. The slope avoids having any significant impact on the uncertainty in the detector angle axis determination, because it is an input parameter in the mapping that has no connection to physical quantities, and does not modify the relation of information in the raw data with the linear detector angle axis. This is not the case for the offset parameter, which directly shifts the axis in relation to the image. This parameter is significant in regards to the accuracy of the detector angle, and this is related to the accuracy of the fitted coordinate mapping function and NCIACA approximation assumptions.

Propogation of uncertainty in the detector angle axis

The error propogation calculations of the last chapter have shown that while γ is a fundamental parameter in the calculation of the detector angle axis, the uncertainty in γ does not actually play a role in the uncertainty in angle, since the data transformed via the distortion correction was corrected with γ as an input parameter that did not have any direct physical implication.

The offset of the detector angle axis itself has an uncertainty given by equation 3.5 with δx^2 given by equation 3.7. As an example, with the parameter choices used earlier in this chapter to find $\delta x^2 = 1.16 \text{ mm}^2$, and using $x=0$ as the experimental situation, this leads to an offset $\delta\Phi$ in the angular axis determination of $3.2 \cdot 10^{-3}$ radians, or about 0.18 degrees. This is the uncertainty introduced in the angle axis from the analysis procedure discussed in this work, and can be considered a typical uncertainty in the angle determined with these methods. The primary effect of this uncertainty is to introduce a finite resolution in momentum space, which will be shown in the next chapter.

Implementation Distortion Correction for the UBC ARPES Chamber

The distortion correction following the discussion up to this point was implemented as a collection of software objects that were written in the IDL programming language. Each object has a specific purpose, and can either be a collection of functions or a self-contained unit which is capable of storing variables and performing series of calculations via indirect calls, for instance, to a single method of the object. This has allowed for relative simplification in the organization and interconnectivity of the final graphic interface software that utilizes the basic functions of the entire distortion correction software hierarchy. A demonstration of the distortion correction software is included in appendix C.

Chapter 6 Mapping to Momentum

In the UBC ARPES system, a detection event will occur at detector angle δ and kinetic energy E_k in the hemispherical analyzer. The momentum of the free electron after it emerges from the sample is the most important information that can be derived from δ and E_k .

Momentum is described as the projection of the momentum into Cartesian directions as simply the multiplication of the magnitude of electron momentum with the unit vector,

$$\vec{k} = \frac{\sqrt{2mE_k}}{\hbar} (\cos \zeta \sin \vartheta \hat{j} + \sin \zeta \sin \vartheta \hat{k} + \cos \vartheta \hat{i}) \quad (6.1)$$

where it is apparent that ϑ is the polar angle and ζ is the azimuthal angle in the usual spherical coordinates. Cast in this form it is analogous to the quantum number $k(\vec{k})$ describing a scalar(vector) Fourier component parameter of the electron wave function.

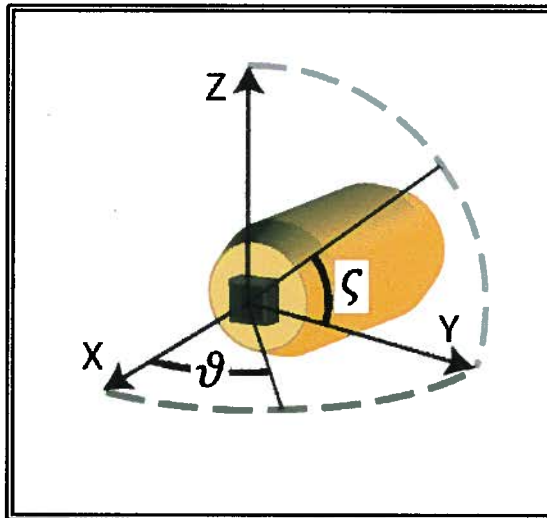


Illustration 6.1. Definition of coordinates that describe the electron emission angle referenced to the sample surface.

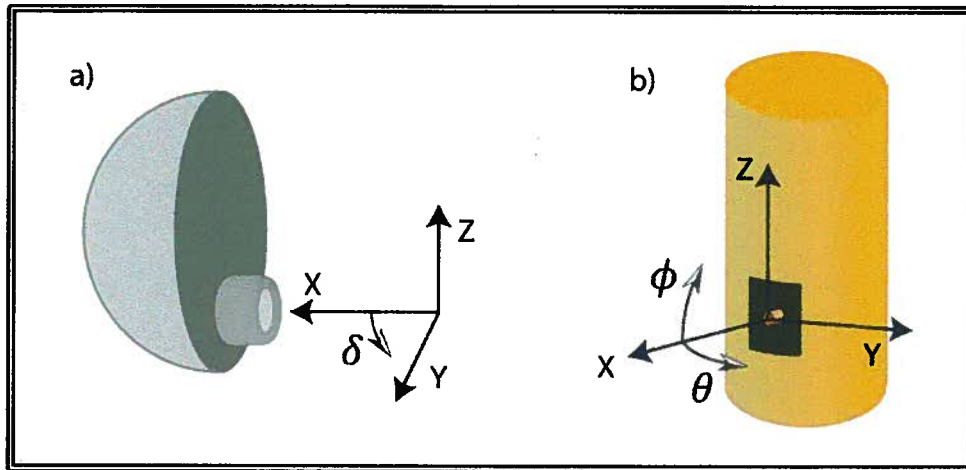


Illustration 6.2. Definition of coordinates that describe (a) the detector angle δ (b) the cryostat angles θ and ϕ .

The momentum of the free electron is determined in the frame of the sample by describing \vec{k} via the construction of a coordinate system on the sample surface separated by rotation transformations from the axes aligned with the IPO symmetry of the detector. The coordinate system is depicted in illustration 6.1. The connection of these coordinates to δ and the kinetic energy can be found with knowledge of the cryostat angles, θ and ϕ , defined by the coordinate system of illustration 6.2. Here we choose the direction in which the x-axis is oriented to be parallel to the optical axis with positive direction into the analyzer entrance, then a right handed coordinate system is constructed by taking the y-axis to be in the plane perpendicular to the x-axis, pointing right when facing the $-x$ direction with positive z-axis vertical and up.

Positive θ is defined here to be the angle from the x-axis towards the y-axis in the x-y plane. Positive ϕ is taken as the angle from the x-axis to the z-axis in the x-z plane. When $\theta = \phi = 0$, the sample-holder is defined to be normal is parallel to the analyzer axis and pointing into the analyzer entrance.

In addition, we must account for angles which define the offset of the sample normal from the zero of cryostat angles. The need for this is experimentally justified by the extreme difficulty that would be encountered in the attempt to adhere a piece of material to a sample-holder in such a way that there is no angular offset between the two. In real situations, this is essentially impossible without elaborate efforts, and in practice it is not difficult to simply account for these angles and correct for them using a reference such as the Fermi surface.

The three crystal-offset angles are defined in an analogous way to the cryostat angles, in the frame of the sample-holder, as θ' and ϕ' along the same directions as theta and phi, respectively. The third angle β corresponds to a rotation of the sample-holder in the y-z plane of the sample-holder coordinate system in illustration 6.1.

Rotation Transformation and Solving Momentum

Altogether, there are two cryostat angles, three crystal-offset angles, two emission angles, detector angle, and kinetic energy as parameters, and the goal is to obtain the components of \vec{k} as a function of these parameters. The approach in this undertaking is to begin with a unit vector pointing along the positive x-axis. Two rotation matrices are used to rotate this vector into the direction defined by ζ and ϑ . This is the vector that describes the emission angle in the reference frame of the sample,

$$\vec{v}_{emission} = T_x(-\vartheta)T_z(-\zeta)\hat{i}$$

The rotation operators are defined as,

$$T_x(a) = \begin{bmatrix} 1 & 0 & 0 \\ 0 & \cos[a] & \sin[a] \\ 0 & -\sin[a] & \cos[a] \end{bmatrix}$$

$$T_y(a) = \begin{bmatrix} \cos[a] & 0 & -\sin[a] \\ 0 & 1 & 0 \\ \sin[a] & 0 & \cos[a] \end{bmatrix}$$

$$T_z(a) = \begin{bmatrix} \cos[a] & \sin[a] & 0 \\ -\sin[a] & \cos[a] & 0 \\ 0 & 0 & 1 \end{bmatrix}$$

These operators rotate vectors in a clockwise fashion, which is equivalent to rotating axes in a counter-clockwise direction. The emission vector is then seen to be the rotation of the vector towards the y-axis through a polar angle ζ , followed by a rotation around the x-axis towards the z-axis through an angle ϑ .

The axial system is now rotated so that $\vec{v}_{emission}$, with the sample normal as the x-axis, is redefined as $\vec{v}_{sample\ holder}$. This is accomplished by first rotating the coordinate system

clockwise by angle β around the x-axis. Once the preferred orientation of the y-z plane is defined by the β rotation, we can rotate clockwise by ϕ' about the y-axis, so that the z-axis moves toward the x-axis. Following this, a rotation about the z-axis counter-clockwise by angle θ' rotates the x-axis towards the y-axis. The emission vector in the sample-holder frame is then given by,

$$\begin{aligned}\vec{v}_{sample} &= T_z(-\theta')T_y(\phi')T_x(-\beta)\vec{v}_{emission} \\ &= T_z(-\theta')T_y(\phi')T_x(-\beta)T_x(-\vartheta)T_z(-\zeta)\hat{i}\end{aligned}$$

It can be mentioned that the choice of angle β is arbitrary, as it simply performs the function of rotating the y and z axes in the sample frame, which is just a redefinition of the orientation of the y and z axes in the plane perpendicular to the sample normal. The angle β was in essence chosen to be zero when the original coordinate system was defined, though the choice of any non-zero angle would result in the transformation from angles to \vec{k} identical to offsetting β by a constant. Leaving β as a parameter allows the continuous redefinition of the starting axes, and is useful for instance in aligning with a symmetry axis in the reciprocal crystal.

The mapping of photoemission intensity as a function of kinetic energy, and detector angle to momentum space additionally requires knowledge of the cryostat angles or whatever system dependent angles that give the sample-holder orientation, to describe $\vec{v}_{sample\ holder}$ from the frame of the analyzer. In the UBC ARPES system, these angles are the θ and ϕ cryostat angles. By rotating the coordinate system counter-clockwise about the y-axis by ϕ , and then rotating clockwise by θ about the z-axis, we are in the analyzer frame. Reversing these two rotations, that is to start in the analyzer frame and rotate counter-clockwise about z by θ and clockwise about y by ϕ , will result in the sample-holder frame. Therefore,

$$\begin{aligned}\vec{v}_{analyzer} &= T_z(-\theta)T_y(\phi)\vec{v}_{sample\ holder} \\ &= T_z(-\theta)T_y(\phi)T_z(-\theta')T_y(\phi')T_x(-\beta)\vec{v}_{emission} \\ &= T_z(-\theta)T_y(\phi)T_z(-\theta')T_y(\phi')T_x(-\beta)T_x(-\vartheta)T_z(-\zeta)\hat{i}\end{aligned}\quad (6.2)$$

We can also write $\vec{v}_{analyzer}$ in terms of the detector angle δ since electrons that are detected from the sample have specific emission vectors, given by,

$$\vec{v}_{analyzer} = \cos \delta \hat{i} + \sin \delta \hat{j} \quad (6.3)$$

Equation 6.2 gives the transformation of a simple unit vector into the emission vector of the electron in the frame of the analyzer via the seven angles $\theta, \phi, \theta', \phi', \beta, \vartheta$, and ζ which characterize the cryostat, sample-holder, and sample positions and the electron direction. The angles ϑ and ζ , together the kinetic energy, are directly related to momentum, as can be seen in equation 6.1, and so the expressions for $\vec{v}_{analyzer}$ indirectly relate angle and momentum. In order to obtain a set of equations that directly gives the mapping from angle to momentum, we must replace ϑ and ζ with the components of \vec{k} from 6.1.

Rewriting expression 6.2 with the definition of the rotation operators leads to,

$$\begin{aligned} \vec{v}_{analyzer} = & \begin{bmatrix} \text{Cos}[\theta] & -\text{Sin}[\theta] & 0 \\ \text{Sin}[\theta] & \text{Cos}[\theta] & 0 \\ 0 & 0 & 1 \end{bmatrix} \cdot \begin{bmatrix} \text{Cos}[\phi] & 0 & -\text{Sin}[\phi] \\ 0 & 1 & 0 \\ \text{Sin}[\phi] & 0 & \text{Cos}[\phi] \end{bmatrix} \cdot \begin{bmatrix} \text{Cos}[\theta'] & -\text{Sin}[\theta'] & 0 \\ \text{Sin}[\theta'] & \text{Cos}[\theta'] & 0 \\ 0 & 0 & 1 \end{bmatrix} \\ & \cdot \begin{bmatrix} \text{Cos}[\phi'] & 0 & -\text{Sin}[\phi'] \\ 0 & 1 & 0 \\ \text{Sin}[\phi'] & 0 & \text{Cos}[\phi'] \end{bmatrix} \cdot \begin{bmatrix} 1 & 0 & 0 \\ 0 & \text{Cos}[\beta] & -\text{Sin}[\beta] \\ 0 & \text{Sin}[\beta] & \text{Cos}[\beta] \end{bmatrix} \\ & \cdot \begin{bmatrix} 1 & 0 & 0 \\ 0 & \text{Cos}[\vartheta] & -\text{Sin}[\vartheta] \\ 0 & \text{Sin}[\vartheta] & \text{Cos}[\vartheta] \end{bmatrix} \cdot \begin{bmatrix} \text{Cos}[\zeta] & -\text{Sin}[\zeta] & 0 \\ \text{Sin}[\zeta] & \text{Cos}[\zeta] & 0 \\ 0 & 0 & 1 \end{bmatrix} \cdot \begin{bmatrix} 1 \\ 0 \\ 0 \end{bmatrix} \end{aligned}$$

Expanding and equating this with equation 6.3 we obtain three equations. To simplify the transcription we will take the constant τ to be defined by,

$$\tau \equiv \frac{\sqrt{2mE_k}}{\hbar}, k_x \equiv k_1, k_y \equiv k_2, k_z \equiv k_3 \text{ where } k_i \text{ is the } i^{\text{th}} \text{ component of } \mathbf{k}.$$

Solving for the components of \vec{k} gives one equation for each component,

$$\begin{aligned}
k_x &= \tau (\text{Cos}[\phi']\text{Sin}[\delta - \theta]\text{Sin}[\theta'] + \text{Cos}[\delta - \theta](\text{Cos}[\theta']\text{Cos}[\phi]\text{Cos}[\phi'] - \text{Sin}[\phi]\text{Sin}[\phi'])) \\
k_y &= \tau (\text{Cos}[\beta](\text{Cos}[\theta']\text{Sin}[\delta - \theta] - \text{Cos}[\delta - \theta]\text{Cos}[\phi]\text{Sin}[\theta']) - \text{Sin}[\beta] \cdot \\
&\quad (\text{Sin}[\delta - \theta]\text{Sin}[\theta']\text{Sin}[\phi'] + \text{Cos}[\delta - \theta](\text{Cos}[\phi']\text{Sin}[\phi] + \text{Cos}[\theta']\text{Cos}[\phi]\text{Sin}[\phi']))) \\
k_z &= \tau (\text{Sin}[\delta - \theta](-\text{Cos}[\theta']\text{Sin}[\beta] - \text{Cos}[\beta]\text{Sin}[\theta']\text{Sin}[\phi']) + \text{Cos}[\delta - \theta] \cdot \\
&\quad (-\text{Cos}[\beta]\text{Cos}[\phi']\text{Sin}[\phi] + \text{Cos}[\phi](\text{Sin}[\beta]\text{Sin}[\theta'] - \text{Cos}[\beta]\text{Cos}[\theta']\text{Sin}[\phi'])))
\end{aligned}$$

These three equations, that give the mapping from angles to momentum, are the central result for this chapter. They fully describe the connection between the laboratory reference coordinates and the physically relevant coordinates for material physics and electron band-structure. There is an idealization implied, in that the ϕ acceptance of the analyzer is taken as infinitesimal, which is not exact for real detection systems where some ϕ averaging must always be present.

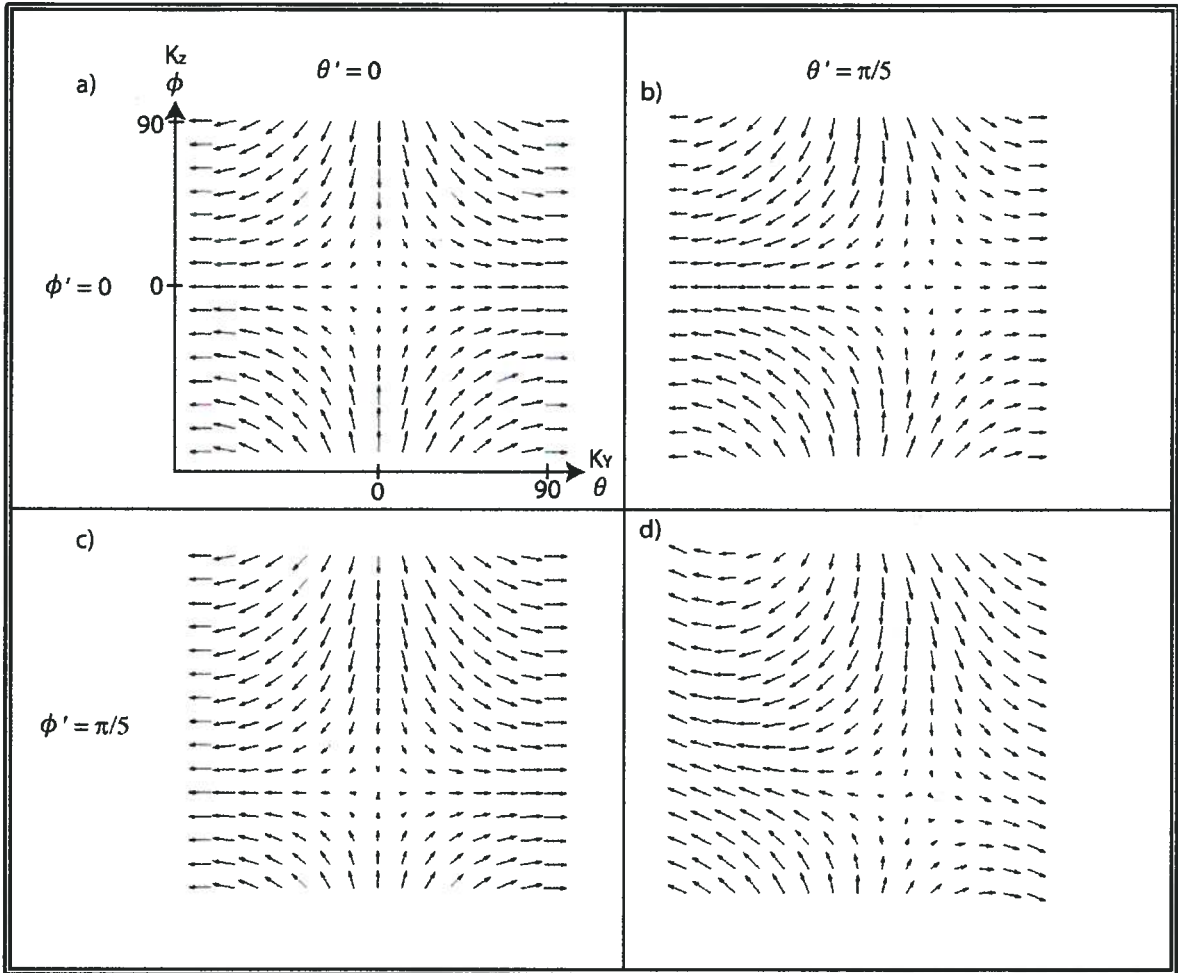


Figure 6.1. Vector plots of $\{K_y, K_z\}$ for $\delta = 0$, for four choices of the crystal offset angles θ' and ϕ' . A shift in the center of the vector field is evident here for crystal angle offsets around 36 degrees, though in practice the offsets are typically less than fifteen degrees.

Figure 6.1 illustrates the effect of the crystal offset angles on the calculated electron momentum from the angle to momentum transformation at the $\delta=0$ detector angle, as θ and ϕ are changed. The effects appear quite complicated due to the large number of angles involved, though the zero momentum position is observed to be offset in a direct fashion by the crystal angles.

As a special case, it sometimes becomes useful to avoid the complication of crystal-offset angles when performing an angle to momentum mapping, such as in situations where the crystal-offset is very small or when speed is important, such as in testing software. By omitting the three crystal-offset angles, and therefore the three matrix operators that accompany them, a greatly simplified set of equations is found that in addition possesses the

property of having an inverse that is a closed formula.

Setting crystal offsets to zero results in,

$$\begin{aligned}k_x &= \tau \cos[\delta - \theta] \cos[\phi] \\k_y &= \tau \sin[\delta - \theta] \\k_z &= -\tau \cos[\delta - \theta] \sin[\phi]\end{aligned}$$

Angles from Momentum

In the situation where we do not include crystal-offsets, we can immediately solve k_2 for the detector angle minus cryostat theta, and use this result to immediately solve for phi in either k_1 or k_3 , so that a reverse of this mapping is simple to obtain. For example, to obtain $(\delta - \theta)$ and ϕ from k_2 and k_3 ,

$$\begin{aligned}(\delta - \theta) &= \sin^{-1} \left[\frac{k_y}{\tau} \right] \\&= \sin^{-1} \left[\frac{\hbar k_y}{\sqrt{2mE_k}} \right] \\&= \sin^{-1} \left[\left(1.95 \frac{\sqrt{eV}}{\text{\AA}} \right) * \frac{k_y}{\sqrt{E_k}} \right]\end{aligned}$$

Then,

$$\begin{aligned}\phi &= \sin^{-1} \left[\frac{-k_z}{\tau \cos[\delta - \theta]} \right] \\&= \sin^{-1} \left[\frac{-\hbar k_z}{\sqrt{2mE_k} \cos[\delta - \theta]} \right] \\&= \sin^{-1} \left[\left(1.95 \frac{\sqrt{eV}}{\text{\AA}} \right) * \frac{-k_z}{\sqrt{E_k} \cos[\delta - \theta]} \right]\end{aligned}$$

Once we have $(\delta - \theta)$ from k_2 , we can see it is a simple matter to insert into the equation for k_3 to obtain ϕ , showing the ease with which this special case can be inverted. Note that the equation for ϕ is singular for $(\delta - \theta) = \pm \pi/2$ in this coordinate system. This singularity poses no problem for the mapping of ARPES data, because there is no reasonable use for data that includes electron emission velocities parallel to the sample surface, for the

reason that such electrons have not even moved out of the sample. Due to the fact that there are always some offset angles to account for, these reverse map functions are of limited use to the experimentalist, though there may be use for simplified theoretical re-creation of an ARPES experiment.

Cryostat Phi Resolution

If the resolution of k_i is examined in the limit of ϕ dominant resolution and zero crystal offsets one obtains that the first and third component of momentum are broadened, and k_2 has no additional broadening.

$$\Delta k_z = |k_z \Delta\phi \text{Cot}[\phi]|$$

Effect of Angular Uncertainty on Momentum Coordinates

If the uncertainty in all parameters is neglected, except for the uncertainty in the detector angle δ , then it is apparent that the uncertainty in the momentum will behave like $\tau \text{Cos}[\delta - \theta]$ or $\tau \text{Sin}[\delta - \theta]$ multiplied by a trigonometric function of the other cryostat and crystal offset angles. The momentum uncertainty is also proportional to the uncertainty in detector axis which was shown to typically be $3.2 \cdot 10^{-3}$ radians. This is a situation where the uncertainty in momentum must necessarily change and a function of momentum. As an example, for the case where the crystal offset angles are zero, the uncertainty in momentum becomes,

$$\Delta k_y = |\tau \Delta\delta \text{Cos}[\delta - \theta]|$$

$$\Delta k_z = |\tau \Delta\delta \text{Sin}[\delta - \theta] \text{Sin}[\phi]|$$

Even without the crystal offset angles, the situation is complicated because the uncertainty depends on both cryostat angle ϕ and electron kinetic energy through τ . Therefore, in general, the uncertainty of momentum space ARPES data is different for every point. In the special case of no crystal offsets, we can expect the highest momentum resolution to occur for k_2 when the kinetic energy is low and θ is near 90 degrees. For k_3 the best resolution occurs when kinetic energy is low, θ is near zero, and ϕ is near zero. The

situation with crystal offsets is necessarily more complicated, but we can already see that the momentum resolution is energy and angle dependent, and that it is different for different momentum directions. From these equations we can see that since the trigonometric function that characterizes the resolution is at most of order one, that the momentum resolution in all directions is at least $\tau \Delta\delta$, so that on average the momentum resolution is bounded by a constant with simple functional form of the square root of electron kinetic energy.

A closer look at the fully crystal offset dependent equations shows that each summation term is accompanied by another where the Sine of some quantity appears in one and the Cosine appears in the other. Overall, for any choice of these angles the summation can only lead to a number of about one, since as one term approaches one the other must go to zero, and the momentum resolution effect is bounded in the same way described for all choices of angles. It is interesting that some angles lead to specific momentum regions with very high precision, since the momentum mapping functions are less dependent on the angles in these regions.

In discussion of this type of uncertainty it can easily be confused with random error that is associated with Gaussian-broadening. The fundamental difference is that here $\Delta\delta$ is essentially a systematic error after a given distortion correction has been carried out. The value is not known and will tend to fluctuate with different fitting procedures and distortion correction mappings that will tend to change slightly on the basis of the use of numerical routines, though $\Delta\delta$ is approximately the same for each point of the distortion corrected data. The main source of the confusion with Gaussian error in momentum space originates from the constant and isotropic $\Delta\delta$ in angle space resulting in a detailed functional form of error in momentum space that varies globally.

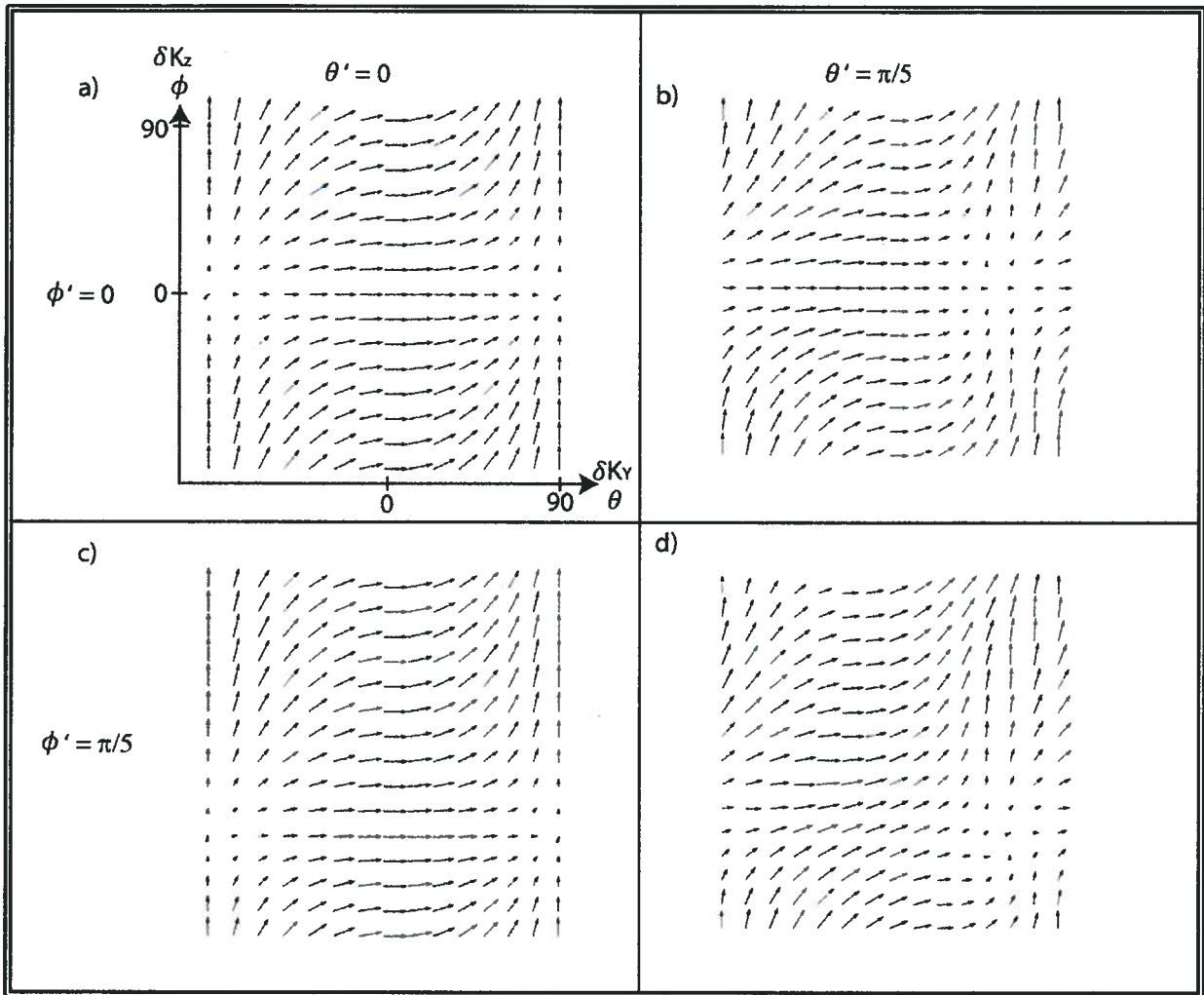


Figure 6.2. The error in momentum coordinates K_y and K_z are shown in both magnitude and direction for crystal offsets up to 36 degrees. The magnitude of the vectors is proportional to the systematic error in the detector angle axis.

The functional form of the error in momentum coordinates does depend on the crystal offset angles. This is depicted in figure 6.2, where it is apparent that special points have almost no dependence on the uncertainty in the detector angle axis offset, since the vector magnitude is near zero based on purely geometrical considerations and born by the trigonometric relations of angle and momentum. Other points have an uncertainty that is essentially only in one momentum direction, so that the directional uncertainty is highly anisotropic for these points. Finally, some cryostat angles lead to uncertainties in momentum coordinates equal for both momentum directions, as shown by vectors that point towards the top right in figure 6.2. The angle dependent error in calculated momentum coordinates means that some portions of the transformed data will depend significantly on systematic error in the

detector angle axis determination, and some special regions will not depend on the detector angle offset.

Chapter 7 Conclusions and Future Applications

This work has introduced calculation methods and experimental procedures for rendering raw ARPES data in a meaningful form. All of the calculations and experimental procedures were developed for the most part independently and the general treatment is fairly self contained. Significant progress has been shown in the ability to characterize the fundamental parameters necessary to translate raw ARPES data into a probe of the electronic structure of materials.

As a result of this work it was shown in a slit array experiment that the accuracies in the determination of the analyzer focal point match the independently calculated values based on essentially random uncorrelated errors in the parameters, resulting in a determination of the focal point at cryostat position $x=1.09\text{mm} \pm 1.07 \text{ mm}$. The experimental error is intrinsically connected to the resolution and feature broadening characteristic of the ARPES detection system. This observation can possibly be used to extend the understanding of the basic broadening properties of the analyzer, with respect to the iso-angle contours for instance, so that the probability distribution for electron and photon detection that forms the basis of photoemission detection as a function of energy and angle can be characterized in terms of the convolution of Gaussian-like distributions.

The focal point and uncertainty determination allows the demonstration of a calculated random offset of the angular axis assigned to distortion corrected ARPES data of 0.2 degrees. In regions where the mapping is well behaved, this is the major uncertainty associated with the distortion correction technique to find the analyzer angle, demonstrating that a precise determination of the angular axis is achievable with the methods developed here. A well-defined analytic angle to momentum mapping has been achieved, in order to render the intensity data versus momentum and energy, also leading to a description of momentum accuracy as a function of momentum. The emerging functional form of momentum precision has its origins in uncertainty acquired in the detector angle axis that comes about in the process of analyzing slit calibration data to determine the detector angle axis.

The software implementation of these methods allows the raw data acquired from the UBC ARPES chamber to be applied to the study of materials. While the overall experimental situation has been shown to be complicated by many technical issues, the progress here is to simplify a number of issues present in the pursuit of high resolution ARPES data. Further

experiments could not be completed on the timeline presented for this work, though plans exist in which these developments will continue in direct analogy with the scientific discussion and literature of electronically two dimensional superconductors.

Many key questions regarding the procedures for handling the raw data acquired in an ARPES experiment must be addressed before one can make use of the wealth of physical information in the data. In performing this type of experiment, it is essential that the desired endpoint is a clearly defined representation of the raw data for facilitation of understanding the underlying physics of materials. This is a task inherent to the use of ARPES as a surface science technique. It is of great use to develop this discussion from a general starting point so that application of the overall method at other experiment facilities is possible. The angle-resolved photoemission spectroscopy apparatus in use at the Quantum Materials Laboratory at the University of British Columbia presents this opportunity, for the connection of this laboratory to imminent developments of ARPES at the Canadian Light Source suggests that application of this work will expedite the development of next-generation ARPES.

References

- Damascelli, A. 2004. Probing the Electronic Structure of Complex Systems by ARPES. *Physica Scripta T109*: 61-74.
- Mattuck, R. *A Guide to Feynman Diagrams in the Many-Body Problem*. Dover, 1992.
- Huefner, S. *Photoelectron Spectroscopy*. Springer Verlag, 1995.
- Goldstein, H. *Classical Mechanics (3rd Edition)*. Addison Wesley, 2001.
- Taylor, J. *An Introduction to Error Analysis*. University Science Books, California, 1997.
- Unser M. 2000. Sampling – 50 Years After Shannon. *Proceedings of the IEEE*, 88(4):569-587.
- Unser M, Aldroubi A, Eden M. 1992. Polynomial Spline Signal Approximations: Filter Design and Asymptotic Equivalence with Shannon's Sampling Theorem. *IEEE Transactions on Information Theory*, 38(1):95-103.
- Unser, M. 1999. Splines: A Perfect Fit for Signal/Image Processing. *IEEE Signal Processing Magazine*, 16(6):22-38.
- Wolberg G. 1996. Recent Advances in Image Morphing. *Proc. Computer Graphics Internat.*, 64-71.
- Thevenaz P, Blu T, Unser M. "Image Interpolation and Resampling." *Handbook of Medical Image Processing*. New York: Academic, 2000 ,chapter 25.
- Ruprecht D, Mueller H. 1995. Image Warping with Scattered Data Interpolation. *IEEE Computer Graphics and Applications*, 15(2):37-43.
- Amidror I. 2002. Scattered Data Interpolation Methods for Electronic Imaging Systems. *Journal of Electronic Imaging*, 11(2):157-176.
- Lax, P. D. 1999. Change of Variable in Multiple Integrals. *Amer. Math. Monthly* 106: 497-501.

Appendix A

SPECS Phoibos 150 Hemispherical Analyzer

The Phoibos 150 Hemispherical Analyzer was manufactured by the SPECS GmbH – Surface Analysis and Computer Technology Company located in Berlin. The path of photo emitted electrons in this detection system begins with incidence into the analyzer entrance. An iris is used to optionally block electrons that fall outside the iris radius around the analyzer entrance central axis. The analyzer has an electron lens with a wide variety of spatial and angle resolved lens modes, which is followed by a series of entrance slits to a hemispherical capacitor used for the selection of electrons within a pass energy (E_P) of an electron kinetic energy (E_K). Upon exiting the hemispherical capacitor, electrons pass through an exit slit, and are then multiplied by a chosen gain in micro-channel plate, then are incident on a phosphor screen. The photons generated by the electron bombardment of the phosphor screen are then captured by a ccd camera (see pixelfly camera).

PCO Pixelfly QE

The PCO Pixelfly QE camera forms the final stage of the detector. The camera is a standard ccd digital camera constructed for low noise and high efficiency characteristics. The ccd array contains 640x480 pixels and is oriented to give the long image axis along the energy direction of the hemispherical analyzer. The camera is located in a position on the hemispherical analyzer such that the entire phosphor screen is captured by the image, hence there is no a priori cropping of the phosphor screen upon final detection. The variable parameters in an ARPES experiment are dwell time and number of exposures, where the first signifies the length in time the ccd array accumulates charge from photodetection before reading the image, and the second refers to the number of images that are averaged into the final image. The camera temperature is stabilized by a dedicated fan that cools the camera housing.

SPECS UVS 300 Very High Intensity UV Lamp

The UVS 300 forms one of the primary light sources for ARPES at the UBC QML. This apparatus guides thermally generated electrons from a hot filament into a discharge region to form a dense plasma along the illumination axis, and is able to achieve high

intensity spectral line photon emission from helium and other gases.

SPECS Toroidal Mirror Monochromator TMM302 R2 and Ellipsoidal Transfer Capillary

Mounted coaxially with the UVS300, the TMM302 R2 uses a toroidal mirror, plane grating, and plane mirror to achieve line selection of the narrow spectral lines output by the high density plasma of the UVS300. This essentially monochromates the photon source in order to facilitate ARPES. The TMM302 R2 itself has a large 500 Liter per second turbo pump attached, which allows a large pressure gradient between the fairly high pressure of the UV lamp and the ultra high vacuum environment of the ARPES chamber. The monochromator is followed by an ellipsoidal capillary with diameter of 1.6 mm. The capillary is designed to allow focusing of the photons in addition to high transmission of around 60 percent, and a focused spot size on the material of interest of about 0.8 mm in diameter.

Electron Gun

The documentation relevant to the SPECS Electron Source was not available at the time of this writing. However, the device was used to illuminate the tungsten wire with a broad range of electron energies simultaneously and performed very well at this task both in terms of energy distribution and beam size as observed in ARPES experiments. The electron source operates through a simple principle of hot filament electron emission with retarding, accelerating, and steering voltage plates. In the experiments carried out in this work the electron energy was set to a distribution centered on 1 keV of energy and beam size was set to less than 0.1 mm in radius.

Cryostat

The cryostat component of the UBC ARPES apparatus was designed primarily as a result of efforts by UBC PhD student Jeff Mottershead. The cryostat has a changeable sample holder, with the sample position aligned with a tungsten wire that was used in this project for the slit correction calibration experiments and theory. Additionally, the cryostat possesses the ability to rotate the sample holder along the cryostat angle axes $\pm 30^\circ$ in ϕ and more than the sufficient $\pm 90^\circ$ in θ (see chapter six for definition of angles). The angular degrees of freedom

are supplemented with translational degrees of freedom x,y,z (see chapter 3 for definition of directions).

Appendix B

The method to obtain a functional relationship for intensity conservation by taking the limiting case of small integration window in equation __ will be examined in this section.

This method would proceed in the following way,

$$\begin{aligned}\lim_{\epsilon \rightarrow 0} \left(\int_a^{a+\epsilon} I(s) ds \right) &= \lim_{\epsilon \rightarrow 0} \left(\int_{x(a)}^{x(a+\epsilon)} I(x'(t)) \frac{dx'(t)}{dt} dt \right) \\ &\cong I(a)\epsilon \cong I(a) \cdot \epsilon \cdot \left. \frac{dx'(t)}{dx} \right|_{x(a)} \\ &\rightarrow \left. \frac{dx'(t)}{dx} \right|_{x(a)} \cong 1\end{aligned}$$

This result does not make any sense, since there is no prior condition that x' is to even necessarily be linear. What can be seen is that the second step is only a valid statement in the limit that ϵ becomes infinitesimally close to zero. If the last statement proves to be true, then there is some validity away from $\epsilon = 0$, but the last statement itself implies that the mapping is just the trivial function $x'(x) = x$. The result is that the small integration window limit does not produce a functional relationship for intensity conservation unless the mapping is trivial.

Appendix C

It is the purpose of this appendix section to illustrate the software procedure in its currently implemented form. The underlying computer code will not be discussed in detail here, since it will not expand the discussion beyond the descriptions of methods already provided in the body of this work. A series of illustrations will be presented, which show how the user interacts with the software, and all illustrations are basically “screen shots” of the software in use on a data set. All software is written in the ITT IDL language.

The first illustration displays the slit correction data, and the way in which the unnecessary energy regions are cropped from the data set. This is achieved with vertical line cursors that enclose the desired region of the data for further processing. The second step shows another cropping window that allows the user to select the angular regions of interest by creating a line through the top two and bottom two white-cross cursors. The regions above and below are removed from the data set. After this the effect of the cropping is shown, and the required user input of number of iso-angle contours and distance of the sample to the slit array. The next step is fitting the contours by adjusting sampling, smoothing, and region size parameters, and the results are shown. Finally, the result of the distortion correction on the slit correction data and data from a material sample is shown.

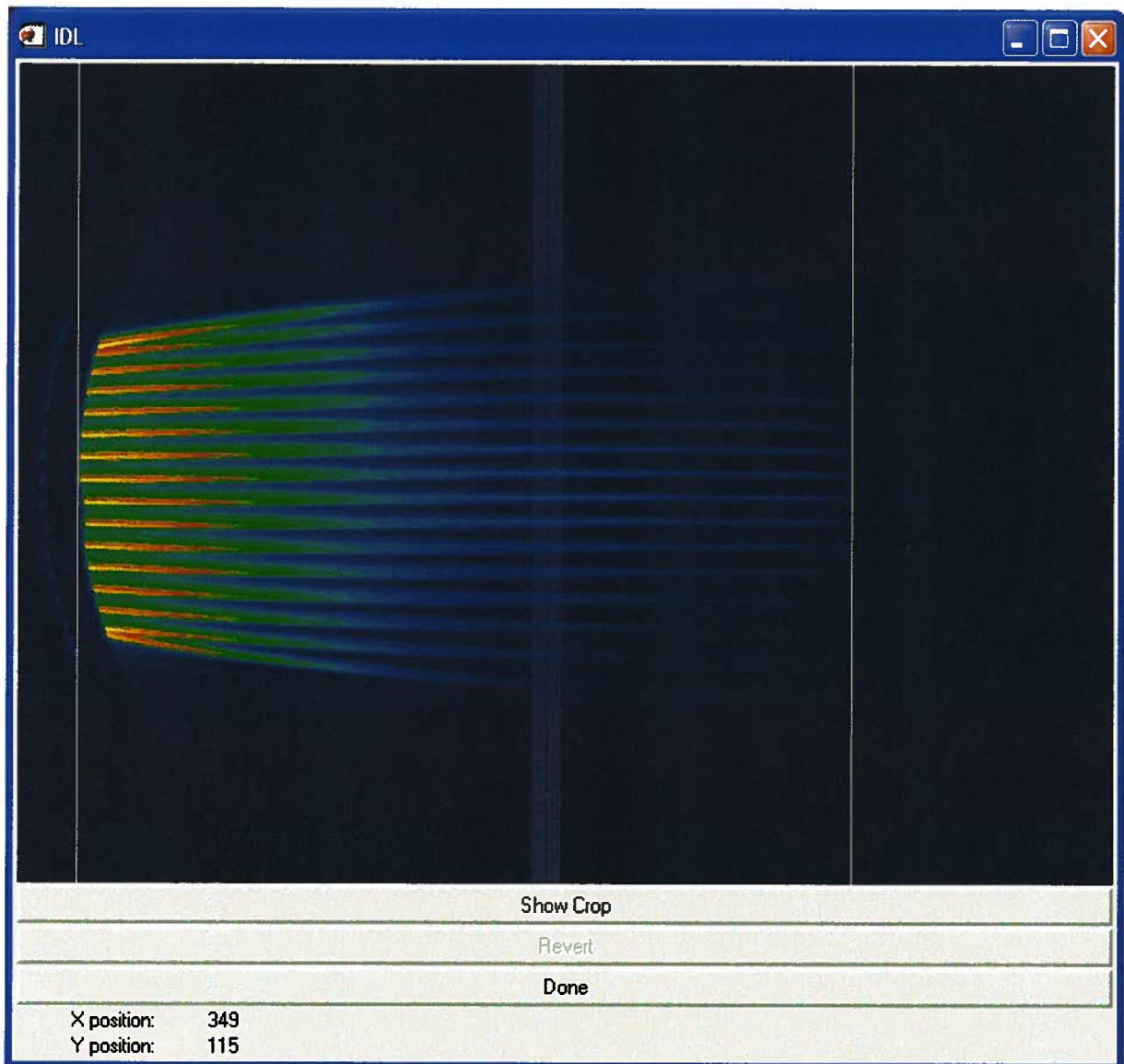


Illustration C.1. The energy direction cropping of the slit correction data. Crop, revert, and done are buttons that the user selects, and the cursor position is continuously displayed.

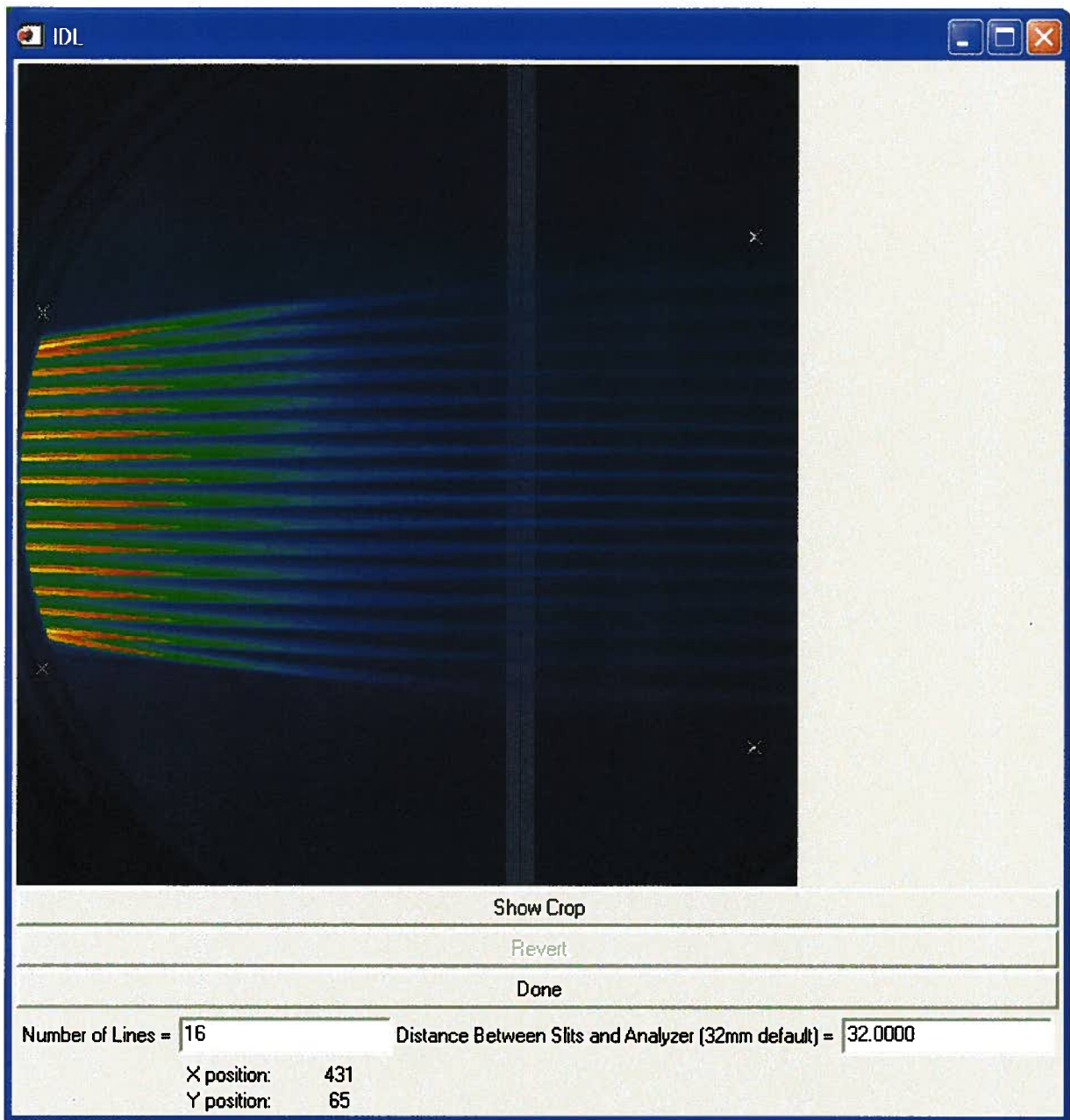


Illustration C.2. Angular direction cropping by construction of lines through the cursors. The number of contours, or lines, is input by the user, as well as the distance between the sample and the slit array.

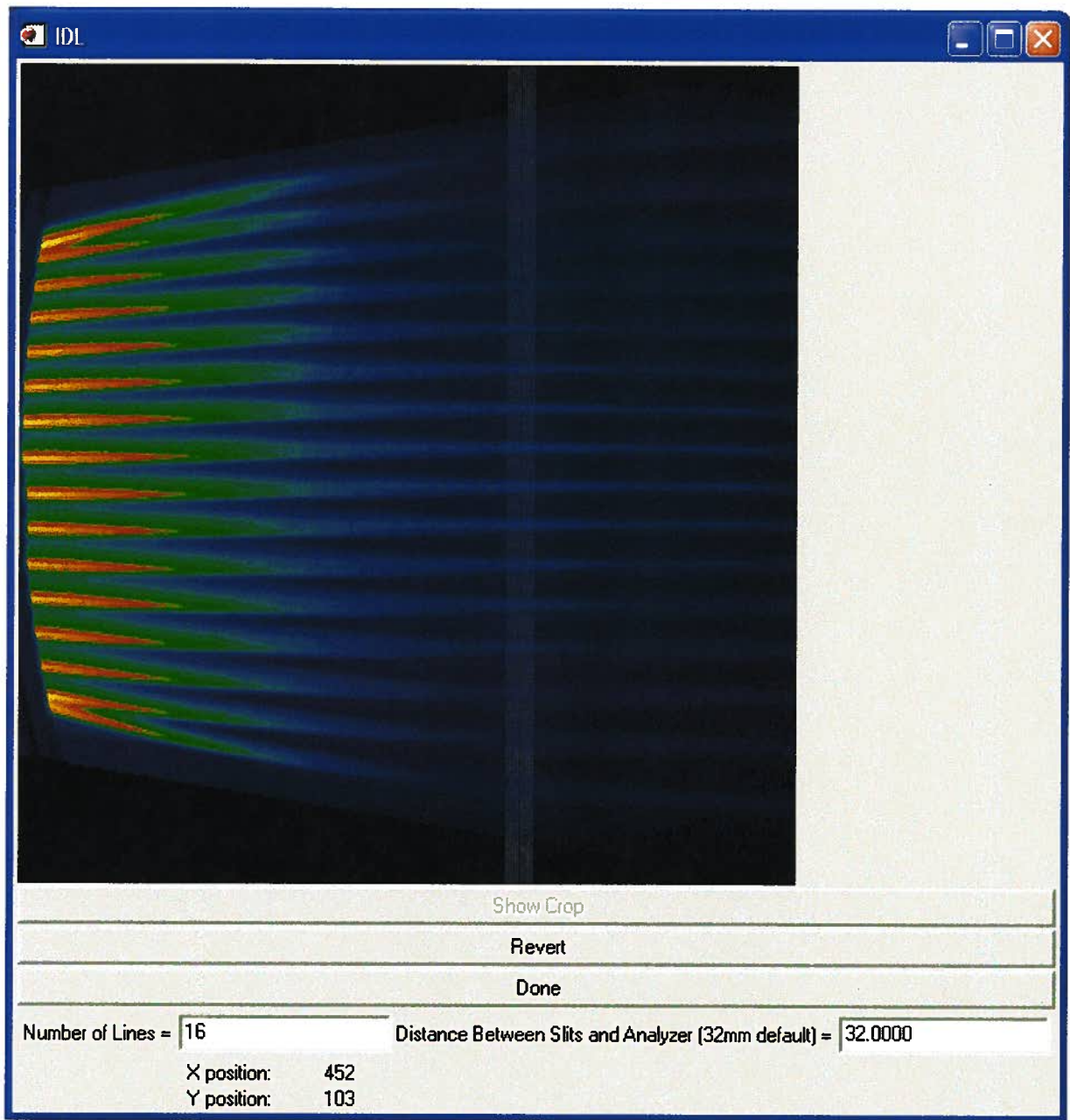


Illustration C.3 The result of the crop settings in illustration C.2.

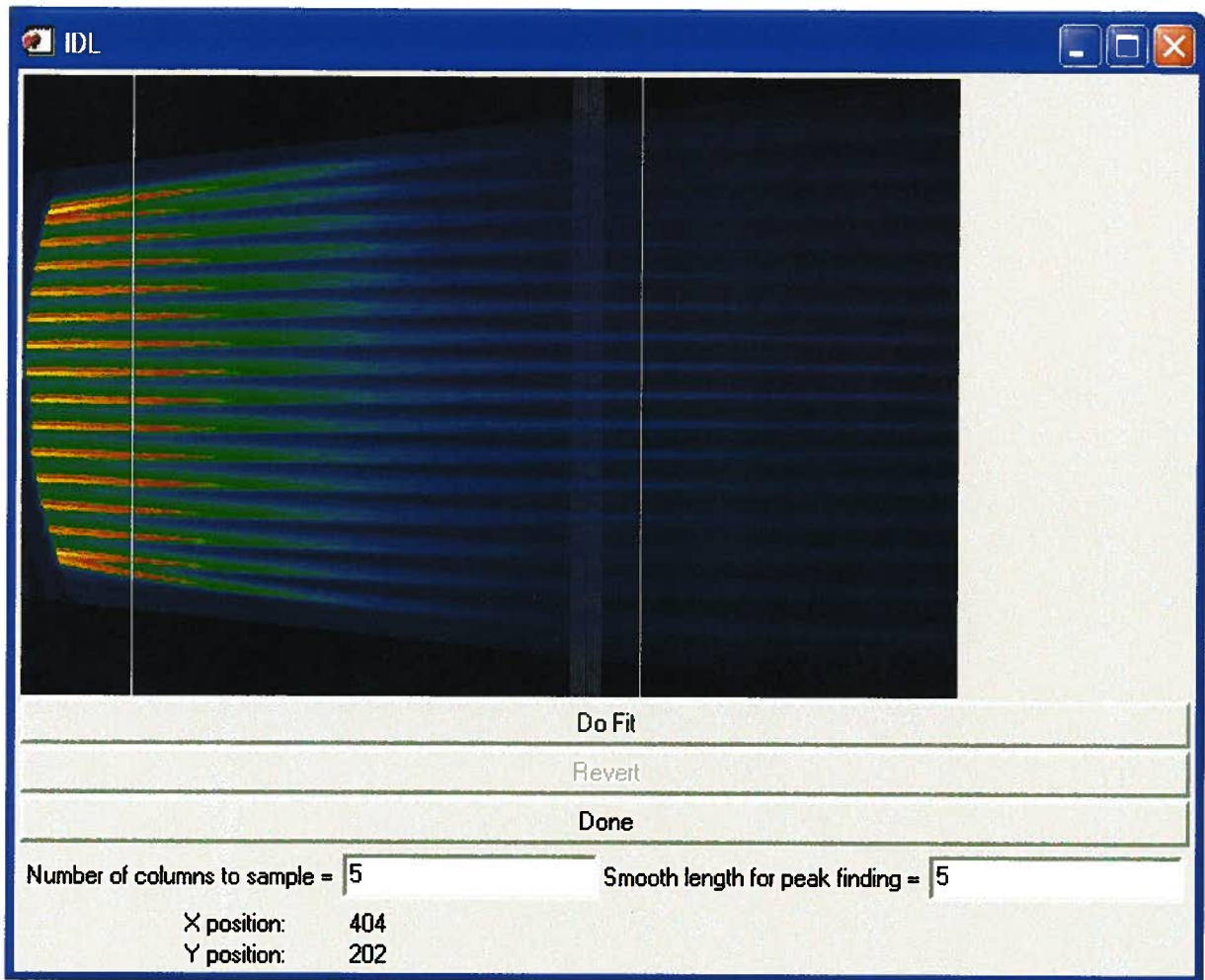


Illustration C.4. The energy region for fitting the contours is shown between the vertical white lines. The number of points to sample for each contour is input, as well as a smooth window size for increasing accuracy when random noise in the data becomes important.

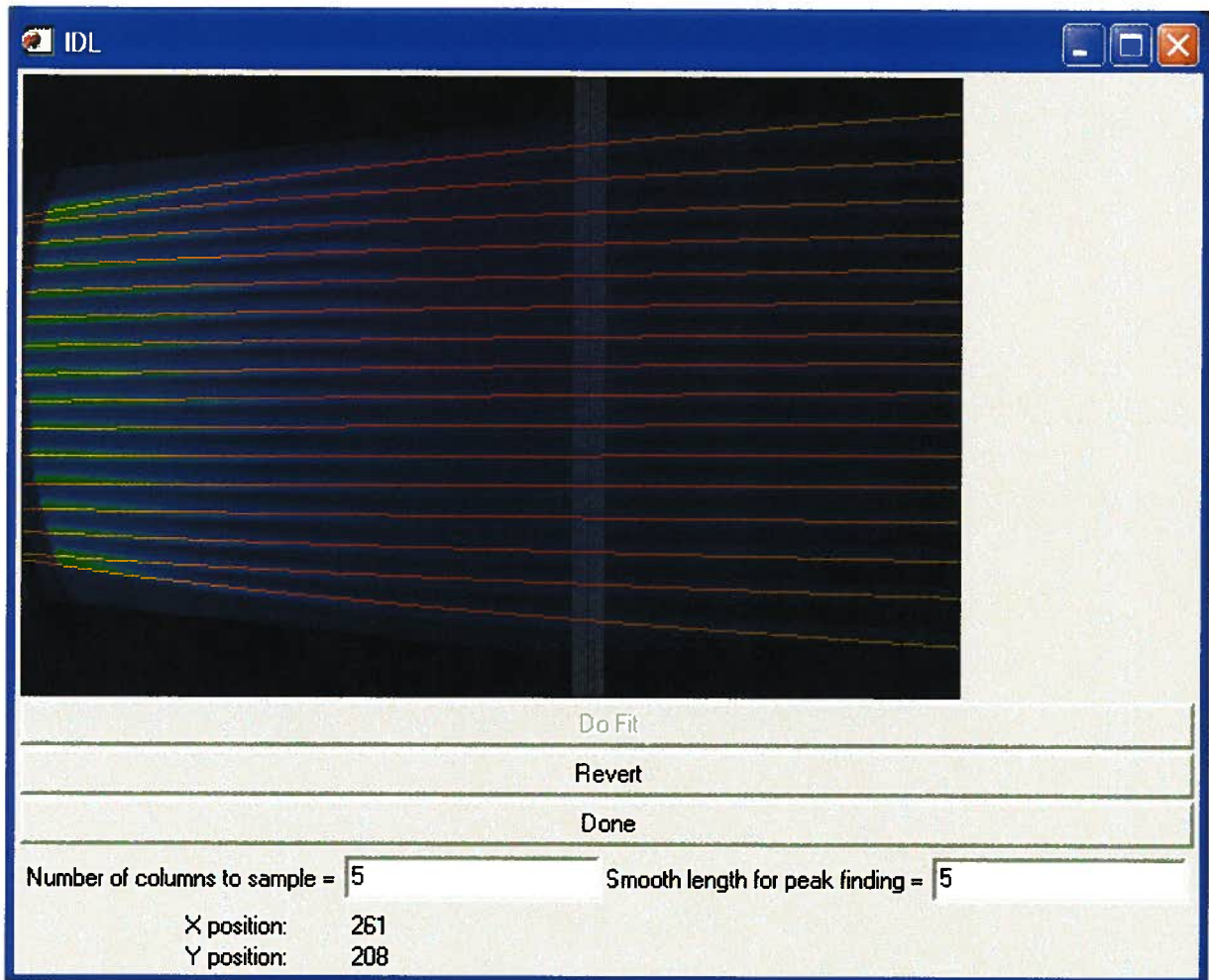


Illustration C.5. The results of the settings of illustration C.4 after fitting the contours. The agreement is quite good for these settings.

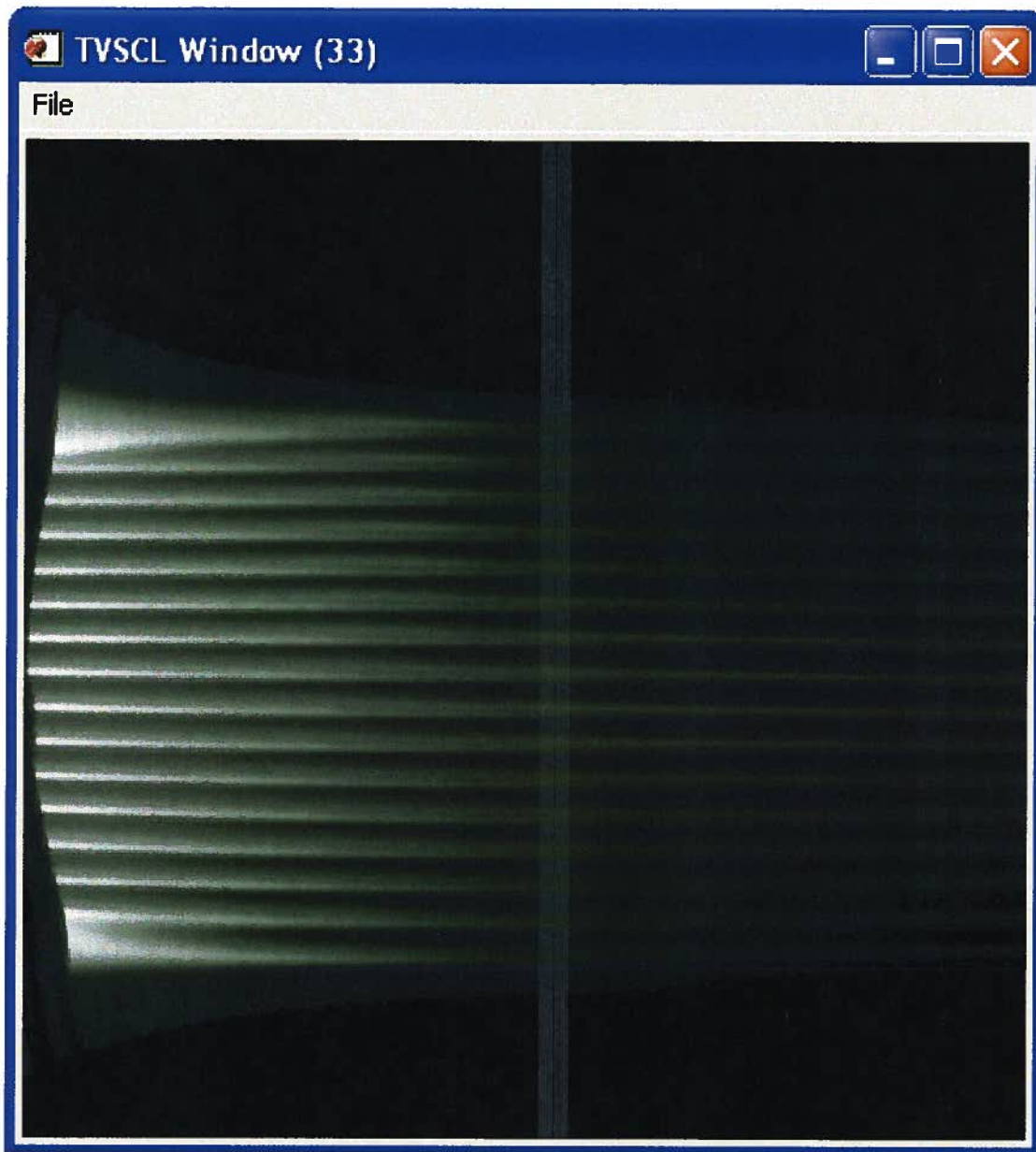


Illustration C.6. A rendering of the slit correction data after is has been corrected with the distortion correction constructed from the previous steps. Notice that some aberration from occurs in the region of lower kinetic energy and large angle in this analyzer lens mode. This is an effect resulting from the iso-angle contours approaching intersection in this region.

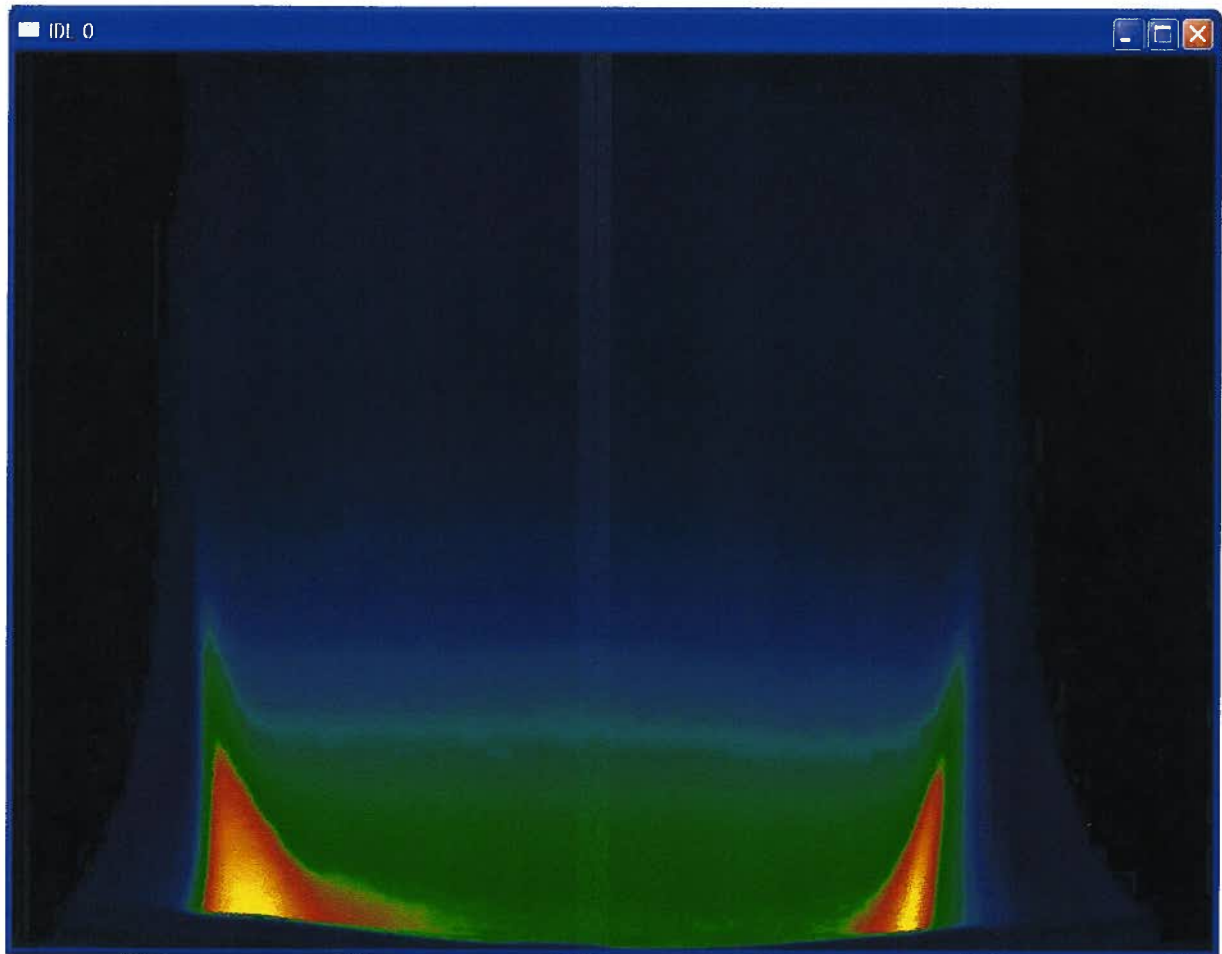


Illustration C.7. The distortion correction applied to a single data image that was taken just after the slit correction data.